



Computational engineering of the oxygen electrode-electrolyte interface in solid oxide fuel cells

Cheng, Kaiming; Xu, Huixia; Zhang, Lijun; Zhou, Jixue; Wang, Xitao; Du, Yong; Chen, Ming

Published in:
npj Computational Materials

Link to article, DOI:
[10.1038/s41524-021-00584-8](https://doi.org/10.1038/s41524-021-00584-8)

Publication date:
2021

Document Version
Peer reviewed version

[Link back to DTU Orbit](#)

Citation (APA):
Cheng, K., Xu, H., Zhang, L., Zhou, J., Wang, X., Du, Y., & Chen, M. (2021). Computational engineering of the oxygen electrode-electrolyte interface in solid oxide fuel cells. *npj Computational Materials*, 7(1), Article 119. <https://doi.org/10.1038/s41524-021-00584-8>

General rights

Copyright and moral rights for the publications made accessible in the public portal are retained by the authors and/or other copyright owners and it is a condition of accessing publications that users recognise and abide by the legal requirements associated with these rights.

- Users may download and print one copy of any publication from the public portal for the purpose of private study or research.
- You may not further distribute the material or use it for any profit-making activity or commercial gain
- You may freely distribute the URL identifying the publication in the public portal

If you believe that this document breaches copyright please contact us providing details, and we will remove access to the work immediately and investigate your claim.

1 **Title Page**

2 **Computational engineering of the oxygen electrode-electrolyte interface in solid oxide fuel**

3 **cells**

4

5 Kaiming Cheng^{1,2}, Huixia Xu^{2,3,4}, Lijun Zhang⁴, Jixue Zhou^{1,*}, Xitao Wang¹, Yong Du^{1,4}, Ming
6 Chen^{2,*}

7

8 ¹ Shandong Provincial Key Laboratory of High Strength Lightweight Metallic Materials,
9 Advanced Materials Institute, Qilu University of Technology (Shandong Academy of Sciences),
10 Jinan 250014, China

11 ² Department of Energy Conversion and Storage, Technical University of Denmark, Lyngby
12 campus, Kgs. Lyngby 2800, Denmark

13 ³ Engineering Research Center of Failure Analysis and Safety Assessment, Shandong Analysis
14 and Test Center, Qilu University of Technology (Shandong Academy of Sciences), Jinan
15 250014, China

16 ⁴ State Key Laboratory of Powder Metallurgy, Central South University, Changsha 410083,
17 China

18

19 * Corresponding authors: minc@dtu.dk (M. Chen), zhoujx@sdas.org (J.X. Zhou)

20

1 **Abstract**

2 The $\text{Ce}_{0.8}\text{Gd}_{0.2}\text{O}_{2-\delta}$ (CGO) interlayer is commonly applied in solid oxide fuel cells
3 (SOFCs) to prevent chemical reactions between the $(\text{La}_{1-x}\text{Sr}_x)(\text{Co}_{1-y}\text{Fe}_y)\text{O}_{3-\delta}$ (LSCF) oxygen
4 electrode and the Y_2O_3 -stabilized ZrO_2 (YSZ) electrolyte. However, formation of the YSZ-CGO
5 solid solution with low ionic conductivity and the SrZrO_3 (SZO) insulating phase still happens
6 during cell production and long-term operation, causing poor performance and degradation.
7 Unlike many experimental investigations exploring these phenomena, consistent and quantitative
8 computational modeling of the microstructure evolution at the oxygen electrode-electrolyte
9 interface is scarce. We combine thermodynamic, 1D kinetic and 3D phase field modeling to
10 computationally reproduce the element redistribution, microstructure evolution and
11 corresponding ohmic loss of this interface. The influences of different ceramic processing
12 techniques for the CGO interlayer, i.e. screen-printing and physical laser deposition (PLD), and
13 of different processing and long-term operating parameters are explored, representing a
14 successful case of quantitative computational engineering of the oxygen electrode-electrolyte
15 interface in SOFCs.

16

17 **Keywords:** solid oxide fuel cells; cathode degradation; YSZ-CGO interdiffusion; SrZrO_3
18 formation; numerical simulation

19

1 Introduction

2 Owing to the advantages of high energy efficiency, broad fuel options, low pollutant
3 emissions and scalable stacks, Solid Oxide Fuel Cells (SOFCs) are attracting increasing attention
4 in the clean and efficient generation of electrical power from renewable sources. However, a
5 worldwide commercialization of SOFCs is hindered due to problems induced by the high
6 operating temperature, i.e. high material cost and materials degradation during long-term
7 operation. Within the past two decades, significant progress has been made in the selection of
8 suitable materials of SOFCs to reduce operating temperature from about 1000 °C to 500–800 °C,
9 of which the latter is known as the Intermediate Temperature SOFCs (IT-SOFCs) ^{1,2}.

10 Generally speaking, the structure of an SOFC cell consists of a dense electrolyte
11 sandwiched by two porous electrodes (cathode and anode). The electrolyte transports oxygen
12 ions from the cathode, where the oxygen is being reduced into oxygen ions, to the anode. High
13 ionic conductivity is an important prerequisite when selecting the electrolyte materials. 8 mol.%
14 yttria stabilized zirconia (8YSZ) is the most widely used electrolyte material so far. Within the
15 intermediate temperature range, gadolinia-doped ceria (CGO) with high ionic conductivity is
16 also regarded as a good electrolyte material for IT-SOFCs, though it may exhibit a minor degree
17 of electronic conductivity at temperatures above 550 °C, reducing the SOFC efficiency ³. The
18 cathode is devoted to reducing oxygen molecules into O²⁻ ions. For IT-SOFCs, the
19 (La_{1-x}Sr_x)(Co_{1-y}Fe_y)O_{3-δ} (LSCF) perovskite with mixed ionic and electronic conductivity
20 (MIEC), good catalytic properties, and good stability has been widely adopted as the cathode
21 material ^{4,5}. Unfortunately, LSCF reacts with YSZ, forming insulating phases of La₂Zr₂O₇ and
22 SrZrO₃ ⁶. A reaction barrier layer made from CGO is often required. The anode material should
23 possess high electronic conductivity and good electro-catalytic activity for fuel oxidation and

1 electrons release. The most commonly used anode material for IT-SOFCs is Ni-YSZ cermet
2 since its invention in 1970, and this situation seems to remain until considerable improvement is
3 reached in the future development of oxide-based anode materials ². In addition to the
4 outstanding performance of the individual materials mentioned above, good mechanical stability
5 and chemical inertness between each component of IT-SOFCs are stringent requirements to
6 develop high performing and durable full cells ⁷. Considering these, the anode-supported Ni-YSZ
7 (anode)/YSZ (electrolyte)/CGO (barrier)/LSCF (cathode) cells are the state of art IT-SOFCs
8 having promising initial performance in the desired temperature range ^{5,8}.

9 The LSCF cathode suffers from performance degradation, which to a large extent is
10 caused by phase transformation or microstructural changes. Apart from the degradation processes
11 in LSCF itself, such as Cr poisoning, sulfur poisoning, coarsening of the microstructure, and loss
12 of conductivity etc. ⁸⁻¹², interactions of the YSZ electrolyte with the CGO barrier as well as the
13 LSCF cathode are two important contributors to the degradation ¹³⁻¹⁶. In an IT-SOFC with the
14 LSCF cathode, the CGO barrier layer is introduced to limit the inter-diffusion and reaction
15 between the LSCF cathode and the YSZ electrolyte, which otherwise will lead to formation of
16 insulating phases, e.g. $\text{La}_2\text{Zr}_2\text{O}_7$ (LZO) and SrZrO_3 (SZO). CGO is chosen as the material for the
17 barrier layer, not only due to its high ionic conductivity at intermediate temperature range as
18 mentioned above, but also due to its good chemical and thermomechanical compatibility with
19 YSZ and LSCF ^{13,17-20}. The literature reported CGO barrier layer is effective, but not yet
20 sufficient to completely stop the inter-diffusion and formation of zirconate phases. The above
21 degradation phenomena still happen in IT-SOFCs with LSCF cathode during either cell
22 fabrication or long-term operation as described further below.

23 In order to fabricate the YSZ (dense)/CGO (preferably dense)/LSCF (porous) structure,

1 wet deposition techniques, e.g. screen printing, spray deposition, and dip coating, are commonly
2 employed. Usually, a two-step sintering is performed, during which the inter-diffusion and
3 reactions already take place, as illustrated in Fig. 1. In this work, the fuel electrode side is not
4 taken into consideration. On the oxygen electrode side, we divide the relevant cell production
5 and operation into three steps. In Step 1, a CGO layer is deposited on the pre-sintered YSZ
6 electrolyte followed by high-temperatures sintering (1200~ 1350 °C) to achieve an effectively
7 dense diffusion barrier layer of CGO. Such high temperature can activate the inter-diffusion
8 processes between CGO and YSZ, which eventually leads to the formation of a $\text{CGO}_x\text{YSZ}_{(1-x)}$
9 solid solution with low ionic conductivity, the well-known Kirkendall voids, or even dopant
10 migration ^{13,14,17,20-22}. In Step 2, a LSCF layer is deposited on the CGO layer, followed by
11 sintering at slightly lower temperature (950 ~ 1150 °C), where the inter-diffusion across the
12 YSZ-CGO interface will still continue, but in a much less degree due to much slower diffusion
13 kinetics. Despite of the existence of the CGO barrier layer, formation of the SZO phase at the
14 YSZ-CGO interface is confirmed by a large amount of experimental investigations so far
15 ^{13,15,30,22-29}. Sr accumulated at the YSZ-CGO interface is believed to diffuse from the LSCF
16 cathode through the CGO barrier layer mainly during the cathode sintering process. During the
17 long-term operation process, i.e. the Step 3 in Fig. 1, the kinetics of Sr diffusion (at 650 ~
18 750 °C) is much slower than in Step 2. But the growth of SZO at the YSZ-CGO interface
19 continues and contributes to the cell long-term degradation when the operation time reaches a
20 magnitude of $>10^3$ h ^{16,24,28}. A dense CGO barrier layer realized without high temperature
21 sintering can effectively limit these inter-diffusion induced degradation processes. Pulsed Laser
22 Deposition (PLD), or Physical Vapor Deposition (PVD), is applicable to produce thin and dense
23 CGO epitaxy on YSZ substrate ^{16,22,23}. Other methods, such as co-firing of the YSZ and CGO

1 layers at reduced temperature utilizing a sintering aid, provides the possibility of compositional
2 and microstructural engineering³¹. Nevertheless, screen-printing is so far the most widely
3 adopted method for producing the CGO barrier layer (and the LSCF cathode as well),
4 considering its high deposition rate and low cost, though it is difficult to achieve fully dense
5 CGO barrier layer as by PLD or PVD.

6 The area specific resistance (ASR) is a common variable to represent the performance of
7 SOFC cells. The ASR can be split into the polarization and the ohmic resistance. The ohmic
8 resistance (ASR_{Ω}) can be ascribed to mainly the electrolyte resistance³². The inter-diffusion
9 between YSZ and CGO and formation of the $CGO_xYSZ_{(1-x)}$ solid solution causes a significant
10 increase in the ohmic resistance. Recent studies indicate that this part of performance
11 degradation depends strongly on the fabrication method of the CGO barrier layer (e.g. screen-
12 printing or PLD etc.) as well as the fabrication conditions (e.g. sintering temperature and time)
13 ^{16,28,29}. The PLD method avoids the barrier layer sintering step (Step 1) where most of the YSZ-
14 CGO inter-diffusion takes place. In addition, it can produce thin dense CGO layer with large
15 grain size to slow down the Sr diffusion, resulting in very little increment in ASR_{Ω} after cathode
16 sintering (Step 2) and after long-term operation (Step 3)¹⁶. For a screen-printed CGO barrier
17 layer, achieving high densification often requires high sintering temperature (>1200 °C) in Step
18 1. This results in significant YSZ-CGO inter-diffusion and thus increment of ASR_{Ω} . The
19 resulting YSZ-CGO inter-diffusion zone can further influence the Sr diffusion and formation of
20 SZO in Step 2 and 3²⁹. The higher the CGO sintering temperature, the denser the CGO layer, the
21 more the CGO-YSZ inter-diffusion, however the less the Sr diffusion and SZO formation. This
22 makes it difficult to identify appropriate fabrication parameters in order to reach an optimum
23 condition to minimize both the YSZ-CGO inter-diffusion and the SZO formation. Moreover, it is

1 even harder to derive a general rule by making a crosswise comparison among the experimental
2 results existing in the literature, since the fabrication conditions of the tested cells from different
3 labs are hardly the same. Considering the above, computational numerical modeling of the
4 microstructure evolution in SOFCs shall be performed not only to reproduce the kinetic and
5 microstructural changes observed experimentally, but also to correlate with the cell performance,
6 hence be able to provide reliable prediction of cell performance as functions of fabrication and
7 long-term operation conditions. If successful, this will open a new route of computational
8 engineering of the oxygen electrode – electrolyte interface, targeting both superior initial
9 performance and good long-term durability.

10 Recently, the current authors have tried modelling the YSZ-CGO inter-diffusion and thin
11 layer SZO formation at the YSZ-CGO interface ^{33,34}. Several simplifications were made in the
12 model, e.g. consideration of no CGO grain growth during high-temperature sintering and treating
13 the SZO phase as a continuous layer instead of dispersed distribution. These simplifications do
14 not reflect what actually happens in IT-SOFCs. To the best of our knowledge, no other
15 computational study has been reported which models the CGO-YSZ inter-diffusion, Sr diffusion
16 and SZO formation during cell production and long-term operation in a systematic way. This is
17 thus the aim of the current work: i) to develop a set of thermodynamic and diffusion kinetic
18 database providing accurate description of the phase relations and elemental diffusivities in the
19 YSZ-CGO-LSCF system based on the Calculation of Phase Diagram (CALPHAD) approach; ii)
20 to kinetically model the experimentally observed ^{16,24,28} YSZ-CGO inter-diffusion, Sr diffusion
21 across the CGO layer and formation of SZO by performing both one dimension (1D) solid-state
22 reaction and three dimension (3D) phase field simulations; iii) to identify the correlations
23 between the cell fabrication and operation parameters, the microstructures, and the ohmic

1 resistance according to the current simulation results, and compare with the previous
2 experimental findings ²⁹.

3

4 **Results and discussion**

5 Simulation of SZO formation in screen-printed CGO

6 [Figure 2](#) plots the simulated composition profile in ZrO₂-CeO₂-SrO in comparison with
7 previous experimental data measured at the CGO-YSZ interface ranging from 5 to 11 μm ²⁴, for
8 the case of a SOFC with screen-printed CGO barrier layer during the different steps in cell
9 production and long-term operation. In [Fig. 2a](#), the distribution of Ce and Zr after the barrier
10 layer sintering step at 1523 K for 2 h is presented, showing a ~1 μm thick inter-diffusion zone at
11 the interface. We have previously reported a systematic investigation on the interdiffusion
12 process between the YSZ electrolyte and the CGO barrier layer, including both experimental
13 investigations and 1D kinetic modelling ³³. The detail will therefore not be repeated here. [Fig. 2b](#)
14 presents the simulated composition profile after the cathode sintering step at 1373 K for 2 h
15 compared with the experimental data reported by Kiebach et al. ²⁴. An accumulation of Sr on the
16 Ce-rich side of the ZrO₂-CeO₂ interface can be clearly observed from the experiment data and is
17 also predicted by the simulation. Why is Sr not accumulated on the ZrO₂-rich side can be well
18 explained by investigating the Sr diffusion route on the isothermal section of the ZrO₂-CeO₂-SrO
19 system. As can be seen from the phase diagram shown in [Supplementary Figure 1](#), the ZrO₂-SrO
20 binary subsystem represents a direct contact between YSZ and LSCF, where SZO forms due to
21 the reaction between them. When a layer of CeO₂ is placed in between, diffusion of Sr in the
22 Gibbs triangle shall follow the path starting from the SrO corner and going through the SrO-
23 CeO₂ subsystem to reach the ZrO₂-CeO₂ side, as shown in [Supplementary Figure 1](#). Since there

1 is no intermediate reaction in the SrO-CeO₂ system, Sr will first enter the two-phase region of
2 Cubic+SZO. In order to reach the two-phase equilibrium, Sr diffuses from the right boundary of
3 the CeO₂ layer to the Ce-rich part of interdiffusion zone (IDZ), and further reacts with the ZrO₂
4 dissolved in CeO₂ (during the barrier sintering step), and forms SZO in the Ce-rich part of IDZ.
5 As the amount of Sr on the Ce-rich side of IDZ increases, the diffusion front of Sr will finally
6 reach the equilibrium between miscibility gap of Cubic ZrO₂+CeO₂ and SZO, indicating growth
7 of SZO into the YSZ region. As can be seen in Fig. 2c, when the SOFC cell is tested at 973 K for
8 2000 h, the diffusion front reaches the original interface between YSZ and CGO. So for screen-
9 printed CGO barrier layer, the property of CGO and more specifically the IDZ layer which can
10 be controlled by varying the processing conditions, is of great importance with regard to stop or
11 slow down the Sr diffusion and the SZO formation.

12 Formation of SZO is the result of Sr diffusion across the CGO barrier layer to the Ce-rich
13 side of IDZ and reaction with ZrO₂ dissolved in CeO₂, and the process continues during long-
14 term operation at intermediate temperature (Step 3). Fig. 3 shows the simulated amount of
15 formed SZO along the diffusion distance for different operation time at 973 K in the case of
16 screen-printed CGO barrier layer, compared with the systematical investigation by Rinaldi et al.
17 ²⁸. The numerical modeling was performed considering a sintering at 1300°C for 3 h for the 6
18 μm thick CGO barrier layer screen-printed on an 8 μm YSZ substrate, followed by screen-
19 printing and sintering of the LSCF layer at 1100°C for 3 h. The long-term operation was
20 performed at 700°C. The simulated changes in the volume percentage of SZO during long-term
21 test is recorded at 0, 1900, 4700 and 10700 h, achieving a reasonable agreement with the
22 experimental data based upon the segmentation of the low kV ESB and InLens grayscale
23 electrons images, and complemented with 3-D EDX elemental mapping for the 10700 h sample.

1 It can be seen that the peak value (i.e. maximum volume percentage of formed SZO) increases
2 from 3 % at 0 h (after cell production) to 25 % at 10700 h (after 10700 h operation at 973 K).
3 The peak position within the IDZ region moves towards the Zr-rich side, which is consistent with
4 the current finding of the Sr diffusion path. A wider distribution of SZO is predicted based on the
5 current simulation, implying a deeper expansion of SZO into the CGO layer. In addition to the
6 simplifications adopted in current modeling, the discard of elastic strain energy could be one
7 reason for the suppression of SZO expansion in the real case. Our simulation result further
8 demonstrates the applicability of current modeling to simulate the formation of SZO in IT-SOFC
9 in the case of screen-printed CGO barrier layer.

10

11 Simulation of the formation of SZO in PLD CGO

12 [Figure 4](#) plots the simulated SZO formation at the YSZ-CGO interface in the case of PLD
13 CGO, after cathode sintering or during long-term operation. In Figs. [4a and 4b](#), formation of
14 SZO is predicted at the CeO₂-ZrO₂ interface, which is of a reasonably small amount in
15 agreement with the experimental data measured at the CGO-YSZ interface ranging from 5 to 9
16 μm. Comparing with the case of screen-printed CGO barrier layer, i.e. [Fig. 2](#), the PLD CGO
17 layer show a much better effect on hindering the Sr diffusion and the SZO formation. This can
18 also be seen in [Fig. 4c](#) that the accumulation of Sr within the simulated IDZ is very slow (less
19 than 0.3% after 2 h sintering at 1373 K and <0.4% after 1500 h operation at 973 K).

20 The dense CGO barrier layer deposited by the low-temperature PLD technique eliminates
21 CGO–YSZ intermixing due to no high temperature sintering, and also prevents extensive SZO
22 formation. Only the grain boundaries in the epitaxial CGO barrier layer facilitate Sr diffusion to
23 the YSZ electrolyte to form SZO ¹⁶. It is also reported that the SZO grain generated at the

1 quadruple junction of the YSZ and epitaxial CGO grains represents an elongated spreading shape
2 along the CGO–YSZ interface ¹⁶. Fig. 5 presents the 3D phase field simulation of the
3 microstructure evolution during SZO formation at 1373K for 2 h. The simulation results indicate
4 the random formation of SZO at the quadruple junction begins at around 1200 s, during which Sr
5 should diffuse across the CGO barrier layer. The particles merge to form a contiguous region
6 after growth for 1 h, and then grow into elongated spreading shape along the CGO–YSZ
7 interface due to faster grain boundary diffusion of Sr²⁺. The distribution of Sr is scanned along
8 two lines of L1 and L2, where the Sr content differences in the bulk and at grain boundaries is
9 around 1.2 % and is much lower than that in the regions of SZO and SrO. The simulation result
10 reproduces the experimental findings reported in ¹⁶ reasonably well. In Fig. 5, the amount of Sr
11 accumulates within the IDZ is calculated and compared with the result of 1D DICTRA
12 simulation, showing good agreement. These results further prove the current modeling of the
13 SZO formation is also valid in the case of PLD CGO barrier layer.

14

15 Evolution of the ASR_{ohm}

16 Our current model can also be used to estimate the electrolyte resistance after cell
17 production and during cell long-term operation by using Eq. 9. The previous experimental study
18 ²⁹ demonstrates that the CGO sintering temperature strongly influences the microstructure
19 evolution in the YSZ/CGO/LSZF region. It was shown that the SZO formation is largely reduced
20 by a screen-printed CGO diffusion barrier layer sintered at sufficiently high temperature
21 (1400 °C), forming a dense IDZ at the YSZ-CGO interface, resulting in low ohmic resistance
22 after cathode sintering ²⁹. The current work tries to simulate these processes as well as to further
23 study the effect of the barrier layer sintering condition. The numerical modeling is chosen to be

1 identical to Fig. 2, and the simulation conditions are selected to keep consistent with the
2 experiment condition²⁹, where a 5.5 μm thick screen-printed CGO was sintered at 1100, 1250,
3 and 1400 °C for 3 h on a 200 μm thick YSZ substrate. The subsequently screen-printed LSCF
4 layer (on top of the CGO layer) was sintered at 1100 °C for 3 h, and the cell long-term operation
5 was performed at 800 °C. In the present work, DC1, DC2 and DC3 refer to the samples where
6 the CGO layer is sintered at 1100, 1250, and 1400 °C, respectively.

7 Figure 6 gives the calculated ASR_{ohm} in DC1, DC2 and DC3 at the three stages of barrier
8 layer sintering (Step 1), cathode sintering (Step 2) and long-term operation (Step 3). As for Step
9 1, compared with the theoretical ASR_{ohm} ($433 \text{ m}\Omega\cdot\text{cm}^2$) estimated when no IDZ or SZO forms,
10 DC1 and DC2 shows only slight increase in ASR_{ohm} , i.e. $435 \text{ m}\Omega\cdot\text{cm}^2$ for DC1 with a barrier
11 layer sintering temperature of 1373 K and $438 \text{ m}\Omega\cdot\text{cm}^2$ for DC2 with a barrier layer sintering
12 temperature of 1523 K, indicating weak interdiffusion between YSZ and CGO at lower sintering
13 temperature. The ASR_{ohm} of DC3 sintered at 1673 K reaches $461 \text{ m}\Omega\cdot\text{cm}^2$ after the 3-hour barrier
14 layer sintering stage. Figure 7a gives the simulated IDZ thickness for DC1, DC2 and DC3 after
15 the barrier layer sintering at 1100 °C, 1250 °C and 1400 °C, respectively. It is clear that the IDZ
16 thickness increases with the sintering time, and the growth rate increases with the sintering
17 temperature. Higher temperature for barrier layer sintering leads to faster interdiffusion between
18 CGO and YSZ, and hence results in thicker IDZ and higher ASR_{ohm} after Step 1.

19 After Step 2, DC1 then exhibits a dramatic increment in ASR_{ohm} : from $430 \text{ m}\Omega\cdot\text{cm}^2$ to
20 $483 \text{ m}\Omega\cdot\text{cm}^2$, which is close to the experimentally measured value of $481 \text{ m}\Omega\cdot\text{cm}^2$ ²⁹. This
21 increment in ASR_{ohm} is mainly due to the formation of SZO at the CGO-YSZ interface. The
22 amount of Sr accumulated in the IDZ is calculated and presented also in Fig. 7. At this stage, it
23 can be seen that DC1 shows the fastest increment of Sr content, while DC2 accumulates slightly

1 more Sr than DC 3, implying that DC3 has the best ability to resist SZO formation. This is
2 consistent with the predicted ASR_{ohm} of DC2 ($442 \text{ m}\Omega\cdot\text{cm}^2$, increased by $7 \text{ m}\Omega\cdot\text{cm}^2$) and of DC3
3 ($461 \text{ m}\Omega\cdot\text{cm}^2$, nearly unchanged) in Step 2. The current modeling results show a reasonable
4 trend in the case of developing a universal computational model, where all the initial conditions
5 and processing parameters are taken into account. The deviation from the experimentally
6 measured results of DC2 ($485 \text{ m}\Omega\cdot\text{cm}^2$) and DC3 ($431 \text{ m}\Omega\cdot\text{cm}^2$)²⁹ can be partly attributed to the
7 simplifications adopted in our model, where no microstructure information (porosity, size and
8 distribution of SZO etc.) is taken into account. In addition, the calculation of ASR from Eq. 9,
9 which considers parallel distribution of cubic solid solution and SZO to calculate the effective
10 resistivity, could be another source of the ASR deviation. Last, but not the least, the lack of
11 accurate experimental detail in the published literature (due to confidentiality and IPR) is another
12 important factor contributing to the deviation from the experimental results.

13 During long-term operation (Step 3) at 1073 K, DC1 exhibits again the fastest SZO
14 formation. The resulting ASR_{ohm} increases from $483 \text{ m}\Omega\cdot\text{cm}^2$ to $530 \text{ m}\Omega\cdot\text{cm}^2$ after 10000 h.
15 Apparently, DC1 with CGO barrier layer sintered at 1100 °C shows the worst ability to resist the
16 formation of SZO phase in both Steps 2 and 3. Although DC2 shows slightly faster Sr
17 accumulation than DC 3 at the IDZ, it turns out to show the lowest ASR_{ohm} after 10000 h (464
18 $\text{m}\Omega\cdot\text{cm}^2$), since the overall ASR_{ohm} increment in Steps 1 and 2 is the lowest among the three
19 samples. DC3 shows the least Sr diffusion, SZO formation, and thusly the lowest ASR_{ohm}
20 increment from $461 \text{ m}\Omega\cdot\text{cm}^2$ to only $469 \text{ m}\Omega\cdot\text{cm}^2$ after 10,000h, indicating the best performance
21 of preventing ohmic loss caused by SZO formation. The major degradation procedure of DC3
22 should be the very thick IDZ generated in Step 1.

23 For all the three samples of DC1-3, the simulation conditions in Steps 2 and 3 are

1 identical. The different behavior of Sr diffusion and accumulation in IDZ and ASR_{ohm} increase
2 are caused by the different barrier layer sintering temperatures applied in Step 1. Considering
3 that the difference in diffusion rate of Sr in DC1-3 is caused by the different microstructure at the
4 IDZ after Step 1, the grain size can be selected as a microstructure indicator. Our calculated grain
5 size of CGO after Step 1 is shown in Fig. 7b, representing an increasing trend from 0.15 μm at
6 1100 $^{\circ}\text{C}$ to 0.63 μm at 1400 $^{\circ}\text{C}$, in good agreement with the experiment values²⁹. In Fig. 7b, the
7 effective interdiffusion coefficient of Sr in CeO_2 after the barrier sintering (Step 1) are estimated
8 using Eq. 4 at both 1100 $^{\circ}\text{C}$ (the cathode sintering temperature) and 800 $^{\circ}\text{C}$ (the long-term
9 operation temperature). It can be clearly seen that the Sr diffusion slows down by a factor of
10 about 10^5 when temperature decreases from 1100 $^{\circ}\text{C}$ to 800 $^{\circ}\text{C}$, and the degree of interdiffusion
11 decreases when the barrier sintering temperature (T_{Step1}) increase. That is to say that the higher
12 sintering temperature in Step 1 can result in larger grain size in IDZ, better prevention of Sr
13 diffusion and thus less SZO formation.

14 However, based on the current simulation result, the thicker IDZ shown in Fig. 7a
15 generated at higher sintering temperature can lead to significant increase of ASR_{ohm} , e.g. DC3.
16 So both of the two variables, i.e. thickness of IDZ and diffusion of Sr in CGO, shown in Fig. 7a
17 and 7b have complex influence on the formation of SZO and the resulting ASR_{ohm} increase,
18 which should be carefully controlled to reach optimum cell performance. In the case of PLD
19 CGO barrier layer, the absence of Step 1 avoids formation of thick IDZ and the large CGO grain
20 size of $\sim 2 \mu\text{m}$ results in about 10 times slower Sr diffusion than that in screen-printed CGO, as
21 shown in Fig. 7b. Together with the thin PLD CGO layer, the current simulation gives an ASR_{ohm}
22 below $100 \text{ m}\Omega\cdot\text{cm}^2$, as shown in Fig. 4c. In spite of the advantages of PLD CGO barrier layer,
23 screen-printed CGO layer remains the most economic and promising method for the purpose of

1 commercialization. In such case, the current work gives a technical route of computational aided
2 optimization of cell fabrication conditions for the oxygen electrode-electrolyte interface and also
3 a model to predict cell degradation in solid oxide fuel cells.

4 In summary, models are developed to reproduce the YSZ-CGO interdiffusion and the
5 SZO formation at the YSZ-CGO interface in this work. The YSZ-CGO-LSCF system is
6 simplified to the ZrO_2 - CeO_2 - SrO system, accounting for interdiffusion of the major elements (Zr
7 and Ce) and the transportation of Sr from LSCF and reaction with YSZ forming SZO. The
8 CALPHAD-type thermodynamic and diffusion kinetic information of the ZrO_2 - CeO_2 - SrO
9 system is carefully evaluated and used as unique input to all the numerical modeling. Our 1D and
10 3D models reproduce the experimentally observed element distribution and microstructure
11 evolution during the relevant steps in cell production and operation, for both screen-printed and
12 PLD CGO barrier layers, indicating the credibility of our model. The calculated ASR_{ohm} suggests
13 a trackable performance evolution within the oxygen electrode-electrolyte interface during the
14 entire fabrication and long-term operation of SOFCs with the help of computational materials
15 modeling. The two key factors of the cell degradation, i.e. IDZ caused by CGO-YSZ
16 interdiffusion and Sr diffusion induced SZO formation, are analyzed to be strongly dependent on
17 the fabrication condition of CGO barrier layer and trade-off should be made when choosing the
18 optimum processing route. It is expected the current route of computer engineering of the oxygen
19 electrode-electrolyte interface in solid oxide fuel cells can serve as quantitative guidance to the
20 selection of fabrication condition and prediction of cell degradation.

21

22 **Methods**

23 Construction of thermodynamic and diffusion kinetic database

1 One set of CALPHAD-type thermodynamic and diffusion kinetic database is constructed
2 and applied as the accurate numerical input for all the simulations performed in this work. The
3 basic idea of CALPHAD approach is to describe the thermodynamic properties of each phase in
4 a system with a mathematical model containing adjustable parameters, which can be evaluated
5 by the optimization method to fit the model to all available experimental information. It is then
6 possible to calculate phase diagrams as well as thermodynamic properties of all the phases ³⁵.
7 The Compound Energy Formalism (CEF) ³⁶ is widely used in CALPHAD modeling, which is
8 introduced here to describe the Gibbs energy for the phases in the current YSZ-CGO-LSCF
9 system. The general formula of a Gibbs free energy function ${}^0G(T) = G(T) - H^{\text{SER}}$ (lattice
10 stability) for stoichiometric compounds can be expressed as,

$${}^0G^i(T) = A_i + B_iT + C_iT\ln(T) + D_iT^2 + E_iT^{-1} + F_iT^7 + G_iT^{-9} \quad (1)$$

11 where H^{SER} is the weighted molar enthalpy of the stable element reference (SER), the pure
12 element in its stable state at 298.15 K, and T the absolute temperature. The subscript i represents
13 the phase described and $A_i \sim F_i$ are parameters to be optimized. There are nine elements
14 included in the current YSZ-CGO-LSCF system, i.e. Zr-Y-Ce-Gd-La-Sr-Co-Fe-O, and it is an
15 extensive project to establish the thermodynamic database for the entire nine-element system,
16 which is also unnecessary for the current simulation.

17 In the current work, the YSZ-CGO-LSCF system is simplified to a model system of
18 $\text{ZrO}_2\text{-CeO}_2\text{-SrO}$. Specifically, the inter-diffusion between YSZ and CGO can be simplified to the
19 generation of interdiffusion zone (IDZ) between cubic ZrO_2 and CeO_2 , where the two boundaries
20 of IDZ are defined when detecting 0.1 at. % ZrO_2 on the CeO_2 -rich side or 0.1 at. % CeO_2
21 dissolved in the ZrO_2 part. The cubic ZrO_2 and CeO_2 phases can be thermodynamically treated as
22 a single Cubic phase following our previous simulation result ^{33,34}. We then use SrO to represent

1 the LSCF perovskite that provides Sr²⁺ (or Sr) to react with ZrO₂ in IDZ. Such a simplification
 2 can reasonably and sufficiently account for the main purpose of studying the inter-diffusion
 3 between YSZ and CGO, the diffusion of Sr²⁺ (or Sr) through CGO layer, and the formation of
 4 SZO at the YSZ-CGO interface. The end-members of the current ZrO₂-CeO₂-SrO system will
 5 then be used to represent the corresponding component in the YSZ-CGO-LSCF system in the
 6 kinetic modeling. The lattice stabilities of the Cubic, SrO and SZO phases are taken from
 7 previous thermodynamic modeling³⁷⁻³⁹, and are carefully evaluated to construct the current
 8 thermodynamic database as described in the [Supplementary Methods](#). No higher order parameter
 9 is used except for the Cubic phase, in order to describe their mutual solid solubility. The molar
 10 Gibbs energy of the cubic phase can be described as,

$$\begin{aligned}
 G_m^{\text{Cubic}} = & c_{(\text{Zr}^{4+})_1(\text{O}^{2-})_2} {}^0G_{(\text{Zr}^{4+})_1(\text{O}^{2-})_2}^{\text{Cubic}} + c_{(\text{Ce}^{4+})_1(\text{O}^{2-})_2} {}^0G_{(\text{Ce}^{4+})_1(\text{O}^{2-})_2}^{\text{Cubic}} \\
 & + RT \left(c_{(\text{Zr}^{4+})_1(\text{O}^{2-})_2} \ln c_{(\text{Zr}^{4+})_1(\text{O}^{2-})_2} + c_{(\text{Ce}^{4+})_1(\text{O}^{2-})_2} \ln c_{(\text{Ce}^{4+})_1(\text{O}^{2-})_2} \right) \quad (2) \\
 & + c_{(\text{Zr}^{4+})_1(\text{O}^{2-})_2} c_{(\text{Ce}^{4+})_1(\text{O}^{2-})_2} {}^0L^{\text{Cubic}}
 \end{aligned}$$

11 where R is the gas constant, ${}^0L^{\text{Cubic}}$ is the interaction parameter, $c_{(\text{Zr}^{4+})_1(\text{O}^{2-})_2}$ and $c_{(\text{Ce}^{4+})_1(\text{O}^{2-})_2}$
 12 are the mole fraction of cubic ZrO₂ and CeO₂, respectively. The thermodynamic description of
 13 the ZrO₂-CeO₂-SrO system is listed in Table 1, where the sublattice model with charged species
 14 is adopted.

15 The diffusion of Ce and Zr between CGO and YSZ can be treated as in our previous
 16 work^{33,34}. On the other hand, the Sr migration through CGO layer is rather complex, and
 17 different mechanisms have been proposed in the literature, including gas phase diffusion through
 18 the pore phase, surface diffusion or bulk/grain boundary diffusion^{40,41}. For the gas phase
 19 diffusion, it is generally believed that SrO derived from the strontium segregation in LSCF reacts

1 with water vapor to form the volatile $\text{Sr}(\text{OH})_2$ gas species, and afterwards transports in the vapor
2 form and deposits again at the reactive sites as SrO. The fast surface diffusion indicates the
3 transport of Sr^{2+} (or Sr) along the crack wall or the inner surface in the CGO barrier, while the
4 bulk/grain boundary diffusion driven by chemical potential of Sr^{2+} (or Sr) appears to be slower,
5 especially for the bulk diffusion which is significantly slower than the other diffusion
6 mechanisms. These different diffusion mechanisms play different roles, depending on the
7 experimental conditions, such as porosity of the CGO barrier layer, temperature, $P(\text{O}_2)$ and
8 $P(\text{H}_2\text{O})$ etc. However, there is still lack of experimental proof and quantification in the literature
9 on how the different diffusion mechanisms contribute to the overall Sr diffusion. In the current
10 work, instead of quantitatively distinguishing the contributions from different diffusion
11 mechanisms or the form of Sr to transport (as gas species, neutral atoms or cations) which is
12 more or less impossible based on available experimental information, we developed a
13 quantitative description of the overall Sr^{2+} migration and SZO formation by using an “apparent”
14 diffusion coefficient. In terms of the diffusion kinetic data, the Arrhenius expression is sufficient
15 to describe the temperature dependence of diffusivity of each charged species in different phases,
16 i.e.

$$D(T) = D_0 \cdot \exp\left(\frac{-Q}{RT}\right) \quad (3)$$

17 where D_0 is the prefactor and Q is the activation energy. The elemental diffusivity data of the
18 current $\text{ZrO}_2\text{-CeO}_2\text{-SrO}$ system evaluated using previous experimental data ⁴²⁻⁴⁵ are listed in
19 Table 2, presented as the CALPHAD-type atomic mobility functions as input data for the current
20 1D simulation. The methodologies to evaluate atomic mobility and the quality of resulting
21 parameters are detailed in the [Supplementary Methods](#), [Supplementary Figures 2a-2d](#) and
22 [Supplementary Table 1](#). In the current database, the “effective” diffusivity formulated as the

1 Hart's equation ⁴⁶ is used, which consists of two contributing items corresponding to the bulk
2 and grain boundary (gb) diffusion, respectively. As shown in Eq. 4, the grain boundary item is
3 used to account for the faster Sr migration via grain boundary, surface and vapor diffusion
4 without further distinguishing between them, due to lack of precise experimental information.

$$D^{\text{effect}} = \frac{\delta}{d} \cdot D^{\text{gb}} + \left(1 - \frac{\delta}{d}\right) \cdot D^{\text{bulk}} \quad (4)$$

5 where δ and d are the grain boundary thickness and the grain size, respectively. As for δ , a
6 nominal value of 5 to 10 atomic diameter is suggested as in ⁴⁷, and δ is thus assumed to be 1 nm
7 in the current simulation. As for d , only the grain growth in the CGO layer is included in the
8 present database due to the model of 1D simulation, which will be described in detail in the
9 modeling part. The sintering temperature for the YSZ electrolyte layer is in general a few
10 hundred degree higher than that of CGO. We hence assume no grain growth in the YSZ layer
11 during sintering of barrier layer and cathode and during long-term operation (Step 1-3 in Fig. 1).
12 Previous studies ⁴⁸⁻⁵⁰ performed systematic experimental investigations on the grain growth
13 behavior of the CGO system as functions of temperature and time, and proposed the following
14 analytical equation,

$$d^2 = d_0^2 + K_0 t \exp\left(\frac{-Q_g}{RT}\right) \quad (5)$$

15 where d is the average grain size at time t , d_0 is the initial grain size, K_0 is a pre-exponential
16 constant, R is the gas constant, T is the absolute temperature, and Q_g denotes the activation
17 energy for grain growth. According to the previous work ⁵⁰, the parameters in our simulation are
18 set to be $d_0 = 1.5 \times 10^{-7}$ m, $K_0 = 0.04 \text{ m}^2 \text{ s}^{-1}$ and $Q_g = 477 \text{ kJ mol}^{-1}$, respectively.

19

20 1D kinetic modeling

1 As the current YSZ-CGO-LSCF system is simplified to the $\text{ZrO}_2\text{-CeO}_2\text{-SrO}$ model
2 system, the phase relations can be computed based on the current thermodynamic description
3 listed in [Table 1](#)⁵¹. [Fig. 8a](#) shows the calculated isothermal section of the $\text{ZrO}_2\text{-CeO}_2\text{-SrO}$ system
4 at 1523K. The SZO phase is located in the middle of the $\text{ZrO}_2\text{-SrO}$ binary line, while a
5 miscibility gap between cubic ZrO_2 and CeO_2 can be found on the $\text{ZrO}_2\text{-CeO}_2$ side. This
6 miscibility gap of the phase Cubic extends to the $\text{ZrO}_2\text{-SrO}$ side to reach a two-phase equilibrium
7 with the SZO phase.

8 We first construct the 1D numerical model to simulate the elemental interdiffusion and
9 formation of SZO in the $\text{ZrO}_2\text{-CeO}_2\text{-SrO}$ system, considering different methods for fabricating
10 the barrier layers, i.e. the screen-printed CGO and PLD CGO. [Fig. 8b](#) gives the 1D numerical
11 model in the case of the screen-printed CGO barrier layer. The three-step (Steps 1-3) simulation
12 is in correspondence to the three processes described in [Fig. 1](#). In order to guarantee the
13 comparability of the current simulation results with previous experimental data, the simulation
14 conditions are set according to the experimental work²⁴. In Step 1, the initial thickness of ZrO_2
15 and CeO_2 layer is set to be 8 and 6 μm , respectively, representing the initial YSZ electrolyte and
16 the CGO barrier layer. The sintering temperature and time are set to be 1523 K and 2 h. The
17 grain growth in CeO_2 region should be considered due to dramatic increase in grain size during
18 barrier layer sintering at high temperature^{24,48-50}, which has a strong influence on the elemental
19 diffusion behavior²⁹. The reason for no grain growth considered in the ZrO_2 layer is that the
20 YSZ electrolyte layer has been pre-sintered at ~ 1673 K²⁸, resulting in quite large grain size. Co-
21 sintering together the CGO barrier layer at 1523 K will thus not lead to significant grain growth
22 in the YSZ layer. A grain size of 2 μm is adopted for the ZrO_2 region in our model. At the right
23 boundary of the CeO_2 region ([Fig. 8b](#)), the appearance of LSCF cathode is represented by a

1 virtual SrO layer with no thickness and one boundary condition on the activity of SrO phase
2 ($a(\text{SrO})$), which is set to be 0 in Step 1. In Step 2, i.e. the cathode sintering process, the $a(\text{SrO})$ is
3 then set to be 1 and the simulation condition is set to be at 1373 K for 2 h. The grain growth in
4 the CeO_2 region should still be considered in this step. During long-term operation, i.e. Step 3,
5 the grain growth in CeO_2 region is ignored due to the low operating temperature at 973 K. The
6 simulation time is selected to be 2000 h to be the same as reported in ²⁴.

7 [Figure 8c](#) gives the 1D numerical model in the case of PLD CGO barrier layer. The
8 simulation conditions are the same as in the reported experimental work ¹⁶. A CeO_2 barrier layer
9 (representing CGO) with a thickness of 0.6 μm is placed on the right side of the ZrO_2 region (8
10 μm , representing YSZ). Since the PLD CGO barrier layer exhibits an epitaxy microstructure, the
11 grain size of CeO_2 is set to be identical to that of ZrO_2 i.e. 2 μm . The deposition of the PLD CGO
12 layer requires no further high temperature heat treatment (sintering) afterwards. In this case, only
13 two processing steps are considered in our simulation, i.e. Step 2 – Cathode sintering and Step 3
14 – Long-term operation. The simulation conditions are set to be 1373K for 2 h and 973 K for
15 1500 h, for Step 2 and 3, respectively. Similar to the case of screen-printed CGO, the CGO grain
16 growth is considered during the cathode sintering step, and the boundary condition of $a(\text{SrO}) = 1$
17 is applied to represent the presence of the LSCF cathode. The current 1D numerical model is also
18 used to reproduce the change of volume percentage of SZO in IDZ during long-term operation
19 for up to 10700 h determined by focused ion beam-scanning electron microscopy (FIB-SEM)
20 serial sectioning (Fig. 3) ²⁸, as well as to estimate the effect of barrier layer sintering temperature
21 on the ohmic loss to compare with the previously reported data (Figs. 6 and 7) ²⁹. In these cases,
22 the modeling parameters (i.e. thickness of YSZ and CGO, temperature, time etc.) are adjusted
23 according to different experimental conditions adopted in the previous work ^{28,29}.

1 In the current work, the above numerical kinetic modeling is carried out using the
2 DICTRA software package implemented in Thermo-Calc ⁵¹. The homogenization model ⁵² in
3 DICTRA is activated to reveal a good coupling between thermodynamic and diffusion kinetic
4 information in [Tables 1 and 2](#). The non-uniform grid is sufficiently refined close to the ZrO₂-
5 CeO₂ interface region and the right boundary of the CeO₂ region to guarantee numerical stability
6 during simulation, as illustrated in [Figs. 8b and 8c](#). It should be further pointed out that due to the
7 simplification of using an apparent diffusion coefficient to represent the Sr migration, i.e. Eq. 4,
8 in this paper, we refer Sr diffusion all in the form of Sr²⁺ irrespective of the different diffusion
9 mechanisms. The different “effective” diffusion behavior of Sr²⁺ for the 1D cases of screen-
10 printed CGO and PLD CGO are reproduced by considering the evolution of grain size, with no
11 further consideration on the change of porosity. Meanwhile, the current model only includes the
12 effect of temperature and time in the simulation of Sr²⁺ migration and SZO formation during 1D
13 long-term operation stage. The effect of electric boundary conditions on the local $P(O_2)$ at the
14 oxygen electrode–electrolyte interface is not considered in the current frame of calculation, since
15 it would lead to complex phenomenon of simultaneous anion and cation migration induced by
16 both electric and chemical potential gradient, with thermodynamic and kinetic phase
17 transformation due to element redistribution ⁵³. This is also based on considerations that in
18 reality, temperature has even a bigger effect than $P(O_2)$ simply due to fast diffusion kinetics at
19 elevated temperatures. These simplifications adopted in current modeling may cause deviation
20 from experimental data, and continuous efforts are being made to include more variables of real
21 conditions in our future computational engineering studies.

22

23 3D phase field modeling

1 Apart from 1D simulation, the current work takes advantage of the multiphase field
2 model^{54,55} to simulate microstructure evolution and SZO formation in the case of PLD CGO
3 barrier layer. Comparing with the 1-D DICTRA simulation, which is suitable for the simulation
4 of SZO formation in a very large time scale, the phase-field simulation mainly focuses on
5 reproducing the details of microstructure evolution within a short period of time. Since the
6 phase-field simulation is computationally expensive, in this work, it is employed only to describe
7 the SZO formation and growth during Step 2 in the case of PLD CGO layer. In the multiphase
8 field theory, each phase grain α is distinct from the other phases by its individual phase field ϕ_α .
9 Three phases are considered in the current ZrO₂-CeO₂-SrO model system, i.e. the Cubic, SrO and
10 SZO phases. The sum constrain exists as $\sum_{\alpha=1\dots3} \phi_\alpha = 1$. The governing equation for each phase
11 field can be expressed as,

$$\dot{\phi}_\alpha = \sum_{\beta=1\dots N} \mu_{\alpha\beta} \left\{ \sigma_{\alpha\beta} \left[\phi_\beta \nabla^2 \phi_\alpha - \phi_\alpha \nabla^2 \phi_\beta + \frac{\pi^2}{2\eta^2} (\phi_\alpha - \phi_\beta) \right] + \frac{\pi}{\eta} \sqrt{\phi_\alpha \phi_\beta} \Delta g_{\alpha\beta} \right\} \quad (6)$$

12 where $\mu_{\alpha\beta}$ is the interfacial mobility, $\sigma_{\alpha\beta}$ is the interfacial energy, $\Delta g_{\alpha\beta}$ is the local deviation
13 from thermodynamic equilibrium and η is the interface thickness. Evolution of the conserved
14 composition field c_α is coupled to phase field and is governed by,

$$\dot{c}_\alpha = \nabla \cdot \sum_{\alpha=1\dots N} \phi_\alpha D_\alpha^{\text{tot}} \nabla c_\alpha \quad (7)$$

15 [Figure 8d](#) shows the computational domain in our SZO formation model using the phase
16 field method. The cathode sintering step (Step 2) in the case of PLD CGO barrier is selected here
17 to study the typical microstructure evolution during formation of SZO phase at the quadruple
18 junction. Considering the grain size of the YSZ phase and the thickness of the CGO layer in the
19 experimental work¹⁶, a cuboid region of $2 \mu\text{m} \times 1 \mu\text{m} \times 0.5 \mu\text{m}$ is modelled including three
20 layers of ZrO₂ ($1 \mu\text{m}$), CeO₂ ($0.6 \mu\text{m}$) and SrO ($0.4 \mu\text{m}$) from the left to the right side. Grain

1 boundaries are defined in the middle of the ZrO₂ and CeO₂ region forming a quadruple junction
 2 to keep consistent with the experimentally observed CGO epitaxy¹⁶. The current 3D modeling is
 3 carried out using MICRESS⁵⁶, and the grain boundary diffusion model is activated to detect the
 4 faster Sr diffusion along CGO grain boundary and the formation of SZO at the quadruple
 5 junction. Under such circumstance, the total diffusivity D_α in Eq. 7 should contain an extra flux
 6 contributed by grain boundary diffusion, i.e.

$$D_\alpha^{\text{tot}} = D_\alpha^{\text{bulk}} + D_\alpha^{\text{gb}} \quad (8)$$

7 where D_α^{bulk} and D_α^{gb} are bulk and grain boundary diffusivities with the prefactor and activation
 8 energy shown in Table 2. It should be noted that D_α^{gb} contributes to D_α^{tot} only at the phase
 9 interface, since it is also proportional to $\phi_\alpha\phi_\beta$ and will cancel out in the bulk region. In order to
 10 allow for the formation of the SZO phase, the seed density model⁵⁷ is applied by placing
 11 randomly distributed inactive SZO particles in the simulation area with an initial grain radius of
 12 0. The SZO particles at quadruple junction can be stabilized when sufficient amount of Sr is
 13 accumulated to reach the two-phase equilibrium with the Cubic phase as shown in Fig. 8a.

14 In the current work, $\Delta g_{\alpha\beta}$ and D_α can be directly obtained from the thermodynamic and
 15 diffusion kinetic database developed for the ZrO₂-CeO₂-SrO system, as shown in Tables 1 and 2.
 16 Integration of these currently developed thermodynamic and diffusion databases into the 3D
 17 phase-field model can be revealed owing to the good coupling between Thermo-calc and
 18 MICRESS^{51,56}. For simplification, all the phases/grains were assumed to be isotropic. The
 19 interface mobility $\mu_{\alpha\beta}$ for the CGO and YSZ grain boundaries are acquired from literature to be
 20 1.7×10^{-8} and 6.5×10^{-10} cm⁴ J⁻¹s⁻¹, respectively^{58,59}. And the interface energy $\sigma_{\alpha\beta}$ for both
 21 of the CGO and YSZ grain boundaries are set to 3.0×10^{-5} J cm⁻² as reported in literature^{58,59}.
 22 The interface thickness η is set to be 3×10^{-8} m. For all the other interfaces with no

1 experimental data available, $\mu_{\alpha\beta}$ and $\sigma_{\alpha\beta}$ are adjusted to be $1.0 \times 10^{-10} \text{ cm}^4 \text{ J}^{-1}\text{s}^{-1}$ and $2.0 \times$
2 $10^{-5} \text{ J cm}^{-2}$ to simply reach diffusion control of the phase transformation.

3

4 Prediction of ohmic loss (ASR_{ohm})

5 As stated before, the ohmic loss at the oxygen electrode-electrolyte interface of an SOFC
6 cell can be ascribed to mainly the electrolyte resistance. In our simulation, additional
7 contribution to the ASR_{ohm} comes from both the YSZ-CGO IDZ and the SZO ion insulator. We
8 consider an YSZ-CGO electrolyte region in 1D with a thickness of l , which is further split into n
9 small grids. The theoretical ASR_{ohm} can be computed by simply summing up the resistivity of
10 YSZ and CGO layer multiplied by each layer width. When the formation of IDZ and SZO is
11 considered, the phase (volume) fraction and electrical resistance of cubic solid solution and SZO
12 should be first computed separately within each grid. The electrical conductivity of a YSZ-CGO
13 solid solution depending on composition and temperature can be found in previous experimental
14 work ⁶⁰, and the data at 700 and 800 °C fitted using polynomial equations are adopted in this
15 work. The temperature dependent conductivity of SZO has also been reported ⁶¹. Then, we
16 consider a parallel distributed cubic solid solution and SZO to calculate the effective resistivity
17 $R(x)$ of each grid. The ohmic loss of the entire bi-layer electrolyte region is estimated by
18 integrating $R(x)$ along the thickness as follow,

$$ASR_{\text{ohm}} = \int_0^l R(x) dx \approx \sum_1^n \frac{N_{\text{Cubic}} N_{\text{SZO}}}{\sigma_{\text{Cubic}} \sigma_{\text{SZO}}} / \left(\frac{N_{\text{Cubic}}}{\sigma_{\text{Cubic}}} + \frac{N_{\text{SZO}}}{\sigma_{\text{SZO}}} \right) \Delta x \quad (9)$$

19 where σ_{Cubic} and σ_{SZO} are the electrical conductivity of cubic solid solution and SZO,
20 respectively. N_{Cubic} and N_{SZO} are the phase fraction of cubic solid solution and SZO within each
21 grid, which can be calculated based on the currently simulated composition profiles. In this
22 work, the Ohmic loss is calculated based solely on the results of phase fraction obtained from

1 Dictra 1D simulations of Step 1 to 3 for both cases of the screen-printed and PLD CGO barrier
2 layers.

3

4 **Data Availability**

5 The authors declare that the main data supporting the findings of this study are available within
6 the paper. Other relevant data are available from the corresponding author upon reasonable
7 request.

8

9 **Acknowledgement**

10 This work is supported by European Horizon 2020-Research and Innovation Framework
11 Programme (H2020-JTI-FCH-2015-1) under grant agreement No.735918 (INSIGHT project) and
12 by EUDP through the project no. 64017-0011 (EP2Gas). In addition, National Natural Science
13 Foundation of China (No. 51801116 and 52001176), Shandong Province Key Research and
14 Development Plan (No. 2019GHZ019, 2019JZZY010364, 2019JZZY020329) and the Youth
15 Innovation and Technology Support Program of Shandong Provincial Colleges and Universities
16 (No. 2020KJA002) are acknowledged. The authors would like to acknowledge Dr. Arata Nakajo
17 and Dr. Giorgio Rinaldi from EPFL for providing the original FIB-SEM data and fruitful
18 discussion.

19

20 **Competing interests**

21 The authors declare no competing financial or non-financial interests.

22

23 **Author contributions**

1 K.C. and H.X. contributed equally to the work on the methodology, software, formal analysis
2 and writing of the original draft. L.Z. and Y.D. provided the datasets and contributed to the
3 writing and to the formal analysis. J.Z. and X.W. were responsible for writing and funding
4 acquisition. M.C. conceived and coordinated the research project and was responsible for
5 supervision, writing and funding acquisition. All authors reviewed the final manuscript.

6

7 **References**

- 8 1. Menzler, N. H., Tietz, F., Uhlenbruck, S., Buchkremer, H. P. & Stöver, D. Materials and
9 manufacturing technologies for solid oxide fuel cells. *J. Mater. Sci.* **45**, 3109–3135
10 (2010).
- 11 2. Kilner, J. A. & Burriel, M. Materials for Intermediate-Temperature Solid-Oxide Fuel
12 Cells. *Annu. Rev. Mater. Res.* **44**, 365–393 (2014).
- 13 3. Jacobson, A. J. Materials for Solid Oxide Fuel Cells. *Chem. Mater.* **22**, 660–674 (2010).
- 14 4. Petric, A. Evaluation of La–Sr–Co–Fe–O perovskites for solid oxide fuel cells and gas
15 separation membranes. *Solid State Ionics* **135**, 719–725 (2000).
- 16 5. Mai, A., Haanappel, V. A. C., Uhlenbruck, S., Tietz, F. & Stöver, D. Ferrite-based
17 perovskites as cathode materials for anode-supported solid oxide fuel cells. *Solid State*
18 *Ionics* **176**, 1341–1350 (2005).
- 19 6. Yamamoto, O. Perovskite-type oxides as oxygen electrodes for high temperature oxide
20 fuel cells. *Solid State Ionics* **22**, 241–246 (1987).
- 21 7. Marinha, D., Dessemond, L. & Djurado, E. Comprehensive Review of Current
22 Developments in IT-SOFCs. *Curr. Inorg. Chem.* **3**, 2–22 (2013).
- 23 8. Wand, W. & Mogensen, M. High-performance lanthanum-ferrite-based cathode for
24 SOFC. *Solid State Ionics* **176**, 457–462 (2005).

- 1 9. Tu, H. & Stimming, U. Advances, aging mechanisms and lifetime in solid-oxide fuel
2 cells. *J. Power Sources* **127**, 284–293 (2004).
- 3 10. Simner, S. P., Anderson, M. D., Engelhard, M. H. & Stevenson, J. W. Degradation
4 Mechanisms of La–Sr–Co–Fe–O₃ SOFC Cathodes. *Electrochem. Solid-State Lett.* **9**, A478
5 (2006).
- 6 11. Yokokawa, H. *et al.* Thermodynamic and kinetic considerations on degradations in solid
7 oxide fuel cell cathodes. *J. Alloys Compd.* **452**, 41–47 (2008).
- 8 12. Komatsu, T., Chiba, R., Arai, H. & Sato, K. Chemical compatibility and electrochemical
9 property of intermediate-temperature SOFC cathodes under Cr poisoning condition. *J.*
10 *Power Sources* **176**, 132–137 (2008).
- 11 13. Mai, A. *et al.* Time-dependent performance of mixed-conducting SOFC cathodes. *Solid*
12 *State Ionics* **177**, 1965–1968 (2006).
- 13 14. Martínez-Amesti, A. *et al.* Reactivity between La(Sr)FeO₃ cathode, doped CeO₂ interlayer
14 and yttria-stabilized zirconia electrolyte for solid oxide fuel cell applications. *J. Power*
15 *Sources* **185**, 401–410 (2008).
- 16 15. Uhlenbruck, S., Moskalewicz, T., Jordan, N., Penkalla, H. J. & Buchkremer, H. P.
17 Element interdiffusion at electrolyte-cathode interfaces in ceramic high-temperature fuel
18 cells. *Solid State Ionics* **180**, 418–423 (2009).
- 19 16. Knibbe, R. *et al.* Cathode-electrolyte interfaces with CGO barrier layers in SOFC. *J. Am.*
20 *Ceram. Soc.* **93**, 2877–2883 (2010).
- 21 17. Horita, T. *et al.* Ceria-zirconia composite electrolyte for solid oxide fuel cells. *J.*
22 *Electroceramics* **1**, 155–164 (1997).

- 1 18. Tu, H. Y., Takeda, Y., Imanishi, N. & Yamamoto, O. Electrode in Solid Oxide Fuel Cells.
2 *Solid State Ionics* **117**, 277–281 (1999).
- 3 19. Uchida, H. High Performance Electrode for Medium-Temperature Solid Oxide Fuel Cells
4 La(Sr)CoO₃ Cathode with Ceria Interlayer on Zirconia Electrolyte. *Electrochem. Solid-
5 State Lett.* **2**, 428 (2002).
- 6 20. Tsoga, A., Gupta, A., Naoumidis, A. & Nikolopoulos, P. Gadolinia-doped ceria and yttria
7 stabilized zirconia interfaces: regarding their application for SOFC technology. *Acta
8 Mater.* **48**, 4709–4714 (2000).
- 9 21. Mitsuyasu, H. Analysis of solid state reaction at the interface of yttria-doped ceria/yttria-
10 stabilized zirconia. *Solid State Ionics* **113–115**, 279–284 (2002).
- 11 22. Wang, F. *et al.* Sr and Zr diffusion in LSCF/10GDC/8YSZ triplets for solid oxide fuel
12 cells (SOFCs). *J. Power Sources* **258**, 281–289 (2014).
- 13 23. Jordan, N. *et al.* Ce_{0.8}Gd_{0.2}O_{2-δ} protecting layers manufactured by physical vapor
14 deposition for IT-SOFC. *Solid State Ionics* **179**, 919–923 (2008).
- 15 24. Kiebach, R. *et al.* Stability of La_{0.6}Sr_{0.4}Co_{0.2}Fe_{0.8}O₃/Ce_{0.9}Gd_{0.1}O₂ cathodes during sintering
16 and solid oxide fuel cell operation. *J. Power Sources* **283**, 151–161 (2015).
- 17 25. Szasz, J. *et al.* High-Performance Cathode/Electrolyte Interfaces for SOFC. *ECS Trans.*
18 **68**, 763–771 (2015).
- 19 26. Wankmüller, F. *et al.* Correlative tomography at the cathode/electrolyte interfaces of solid
20 oxide fuel cells. *J. Power Sources* **360**, 399–408 (2017).
- 21 27. Matsuda, J. *et al.* TEM and ETEM Study on SrZrO₃ Formation at the LSCF/GDC/YSZ
22 Interfaces. *ECS Trans.* **78**, 993–1001 (2017).

- 1 28. Rinaldi, G. *et al.* Strontium Migration at the GDC-YSZ Interface of Solid Oxide Cells in
2 SOFC and SOEC Modes. *ECS Trans.* **78**, 3297–3307 (2017).
- 3 29. Wilde, V. *et al.* Gd_{0.2}Ce_{0.8}O₂ Diffusion Barrier Layer between (La_{0.58}Sr_{0.4})(Co_{0.2}Fe_{0.8})O_{3-δ}
4 Cathode and Y_{0.16}Zr_{0.84}O₂ Electrolyte for Solid Oxide Fuel Cells: Effect of Barrier Layer
5 Sintering Temperature on Microstructure. *ACS Appl. Energy Mater.* **1**, 6790–6800 (2018).
- 6 30. Chou, J.-T. *et al.* Mechanism of SrZrO₃ Formation at GDC/YSZ Interface of SOFC
7 Cathode. *J. Electrochem. Soc.* **165**, F959–F965 (2018).
- 8 31. Railsback, J., Choi, S. H. & Barnett, S. A. Effectiveness of dense Gd-doped ceria barrier
9 layers for (La,Sr)(Co,Fe)O₃ cathodes on Ytria-stabilized zirconia electrolytes. *Solid State*
10 *Ionics* **335**, 74–81 (2019).
- 11 32. Zhang, Y. *et al.* Recent Progress on Advanced Materials for Solid-Oxide Fuel Cells
12 Operating Below 500 °C. *Adv. Mater.* **29**, 1700132 (2017).
- 13 33. Xu, H. *et al.* Interdiffusion between gadolinia doped ceria and yttria stabilized zirconia in
14 solid oxide fuel cells: Experimental investigation and kinetic modeling. *J. Power Sources*
15 **441**, 227152 (2019).
- 16 34. Cheng, K. *et al.* Numerical Simulation of the SrZrO₃ Formation in Solid Oxide Fuel Cells.
17 *J. Electron. Mater.* **48**, 5510–5515 (2019).
- 18 35. Lukas, H., Fries, S. G. & Sundman, B. *Computational Thermodynamics: The Calphad*
19 *Method.* (Cambridge University Press, 2007).
- 20 36. Hillert, M. The compound energy formalism. *J. Alloys Compd.* **320**, 161–176 (2001).
- 21 37. Du, Y., Yashima, M., Koura, T., Kakihana, M. & Yoshimura, M. Thermodynamic
22 evaluation of the ZrO₂-CeO₂ system. *Scr. Metall. Mater.* **31**, 327–332 (1994).

- 1 38. Risold, D., Hallstedt, B. & Gauckler, L. J. The Strontium-oxygen system. *Calphad*
2 *Comput. Coupling Phase Diagrams Thermochem.* **20**, 353–361 (1996).
- 3 39. Gong, W. P. *et al.* Experimentation and thermodynamic modelling on SrZrO₃. *Trans.*
4 *Nonferrous Met. Soc. China (English Ed.* **17**, 739–743 (2007).
- 5 40. Lu, Z. *et al.* SrZrO₃ Formation at the Interlayer/Electrolyte Interface during (La_{1-x}Sr_x)₁₋
6 _δCo_{1-y}Fe_yO₃ Cathode Sintering . *J. Electrochem. Soc.* **164**, F3097–F3103 (2017).
- 7 41. Darvish, S., Gopalan, S. & Zhong, Y. Thermodynamic stability maps for the
8 La_{0.6}Sr_{0.4}Co_{0.2}Fe_{0.8}O_{3±δ}–CO₂–O₂ system for application in solid oxide fuel cells. *J. Power*
9 *Sources* **336**, 351–359 (2016).
- 10 42. Kilo, M. *et al.* Cation transport in yttria stabilized cubic zirconia: ⁹⁶Zr tracer diffusion in
11 (Zr_xY_{1-x})O_{2-x/2} single crystals with 0.15 ≤ x ≤ 0.48. *J. Eur. Ceram. Soc.* **20**, 2069–2077
12 (2000).
- 13 43. Bekale, V. M., Huntz, A. M., Legros, C., Sattonnay, G. & Jomard, F. Impurity diffusion of
14 cerium and gadolinium in single- and polycrystalline yttria-stabilized zirconia. *Philos.*
15 *Mag.* **88**, 1–19 (2008).
- 16 44. Beschnitt, S. & De Souza, R. A. Impurity diffusion of Hf and Zr in Gd-doped CeO₂. *Solid*
17 *State Ionics* **305**, 23–29 (2017).
- 18 45. Mandt, T. *et al.* Sr-diffusion in Ce_{0.8}Gd_{0.2}O_{2-δ} layers for SOFC application. *Mater. Res.*
19 *Soc. Symp. Proc.* **1542**, 26–31 (2013).
- 20 46. Hart, E. W. On the role of dislocations in bulk diffusion. *Acta Metall.* **5**, 597 (1957).
- 21 47. German, R. M. *Thermodynamic and Kinetic Treatments. Sintering: from Empirical*
22 *Observations to Scientific Principles* (Elsevier, 2014).

- 1 48. He, Z. *et al.* Densification and grain growth during early-stage sintering of Ce
2 $_{0.9}\text{Gd}_{0.1}\text{O}_{1.95-\delta}$ in a reducing atmosphere. *Acta Mater.* **58**, 3860–3866 (2010).
- 3 49. Ni, D. W. *et al.* Densification and grain growth during sintering of porous $\text{Ce}_{0.9}\text{Gd}_{0.1}\text{O}_{1.95}$
4 tape cast layers: A comprehensive study on heuristic methods. *J. Eur. Ceram. Soc.* **33**,
5 2529–2537 (2013).
- 6 50. Ni, D. W., Esposito, V., Foghmoes, S. P. V. & Ramousse, S. Densification and grain
7 growth kinetics of $\text{Ce}_{0.9}\text{Gd}_{0.1}\text{O}_{1.95}$ in tape cast layers: The influence of porosity. *J. Eur.*
8 *Ceram. Soc.* **34**, 2371–2379 (2014).
- 9 51. Andersson, J.-O., Helander, T., Höglund, L., Shi, P. & Sundman, B. Thermo-Calc &
10 DICTRA, computational tools for materials science. *Calphad* **26**, 273–312 (2002).
- 11 52. Larsson, H. & Höglund, L. Multiphase diffusion simulations in 1D using the DICTRA
12 homogenization model. *Calphad* **33**, 495–501 (2009).
- 13 53. Ta, N. *et al.* Numerical simulation of kinetic demixing and decomposition in a $\text{LaCoO}_{3-\delta}$
14 oxygen membrane under an oxygen potential gradient. *J. Memb. Sci.* **548**, 526–539
15 (2018).
- 16 54. Steinbach, I. *et al.* A phase field concept for multiphase systems. *Phys. D Nonlinear*
17 *Phenom.* **94**, 135–147 (1996).
- 18 55. Steinbach, I. Phase-field models in materials science. *Model. Simul. Mater. Sci. Eng.* **17**,
19 073001 (2009).
- 20 56. <http://www.micress.de>.
- 21 57. BOTTGER, B., EIKEN, J. & STEINBACH, I. Phase field simulation of equiaxed
22 solidification in technical alloys. *Acta Mater.* **54**, 2697–2704 (2006).

- 1 58. Chen, P. L. & Chen, I. W. Grain growth in CeO₂: Dopant effects, defect mechanism, and
2 solute drag. *Journal of the American Ceramic Society* vol. 79 1793–1800 (1996).
- 3 59. Dong, Y. & Chen, I. Mobility transition at grain boundaries in two-step sintered 8 mol%
4 yttria-stabilized zirconia. *J. Am. Ceram. Soc.* **101**, 1857–1869 (2018).
- 5 60. Tsoga, A. Total electrical conductivity and defect structure of ZrO₂–CeO₂–Y₂O₃–Gd₂O₃
6 solid solutions. *Solid State Ionics* **135**, 403–409 (2000).
- 7 61. Willy Poulsen, F. & van der Puil, N. Phase relations and conductivity of Sr- and La-
8 zirconates. *Solid State Ionics* **53–56**, 777–783 (1992).

9

1 **Figure Legends**
2

Fig. 1: Schematic diagram of the oxygen electrode-electrolyte interface reactions

The inter-diffusion and reaction processes happening in the YSZ-CGO-LSCF region during cell fabrication (Step1 and 2) and long-term operation (Step 3) of IT-SOFCs with LSCF cathode.

Fig. 2: Composition profiles across the oxygen electrode-electrolyte interface (screen-printed CGO)

Simulated composition profiles (dotted lines) in ZrO_2 - CeO_2 - SrO in comparison with previous experimental data (scattered symbols)²⁴, for the case of a SOFC with screen-printed CGO barrier layer during the different steps in (a and b) cell production and (c) long-term operation. Distance at 0 μm corresponds to the left boundary of the ZrO_2 layer, and the original ZrO_2 - CeO_2 interface is located at 8 μm .

Fig. 3: Simulated and measured SZO formation at the oxygen electrode-electrolyte interface (screen-printed CGO)

Amount of formed SZO after different operation time in the case of screen-printed CGO barrier layer predicted from 1D kinetic modeling (red solid lines), compared with the FIB-SEM investigation (blue dotted lines)²⁸.

Fig. 4: Composition profiles across the oxygen electrode-electrolyte interface (PLD CGO)

(a and b) Simulation (dashed lines) of the SZO formation at the YSZ-CGO interface during cathode sintering (Step 2) and long-term operation (Step 3) in comparison with the experimental data (scattered symbols)¹⁶ (c) Estimated amount of Sr in the simulated IDZ and the corresponding ASR_{ohm} at 700 °C. Distance at 0 μm corresponds to the left boundary of the

ZrO₂ layer in Fig. 2c, and the original ZrO₂-CeO₂ interface is located at 8 μm.

Fig. 5: Phase field simulation of the oxygen electrode-electrolyte interface reactions (PLD CGO)

Simulation of the SZO formation at the YSZ-CGO interface in the case of PLD CGO during cathode sintering at 1373K for 0, 1200, 2400, 3600, 4800 and 7200 s. The size of 3D phase-field simulation area has been shown in the modeling section. The distribution profiles of Sr are scanned along two lines of L1 and L2, and the amount of Sr accumulates within the IDZ is calculated and compared with the result of 1D DICTRA simulation.

Fig. 6: Predicted ASR_{ohm} change resulting from the oxygen electrode-electrolyte interface reactions

Calculated ASR_{ohm} at 800 °C in DC1, DC2 and DC3 at the three stages of barrier sintering (Step 1), cathode sintering (Step 2) and long-term operation (Step 3) and the amount of Sr accumulated in the IDZ, together with the experimentally measured values ²⁹.

Fig. 7: Numerical analysis on changes of the microstructural parameters during the oxygen electrode-electrolyte interface reactions

(a) Simulated IDZ thickness for DC1, DC2 and DC3 after the barrier sintering step at 1100 °C, 1250 °C and 1400 °C. (b) The estimated effective interdiffusion coefficient of Sr in CeO₂ barrier layer at 1073K and 1373K plotted against sintering temperature of Step 1 and the corresponding grain size of CGO. The solid lines show the general trend and the dashed lines are to aid figure analyzation. The error bars show the range of measured grain size reported in literature ²⁹.

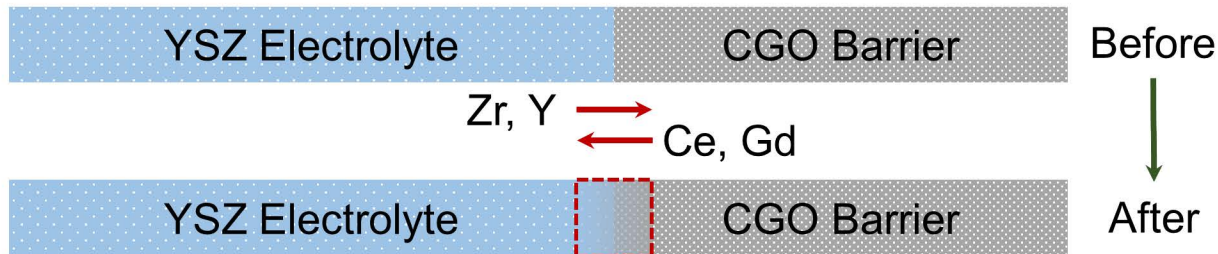
Fig. 8: Models developed for simulating the oxygen electrode-electrolyte interface reactions

(a) Calculated isothermal section of the ZrO₂-CeO₂-SrO system at 1523 K; (b) 1D numerical

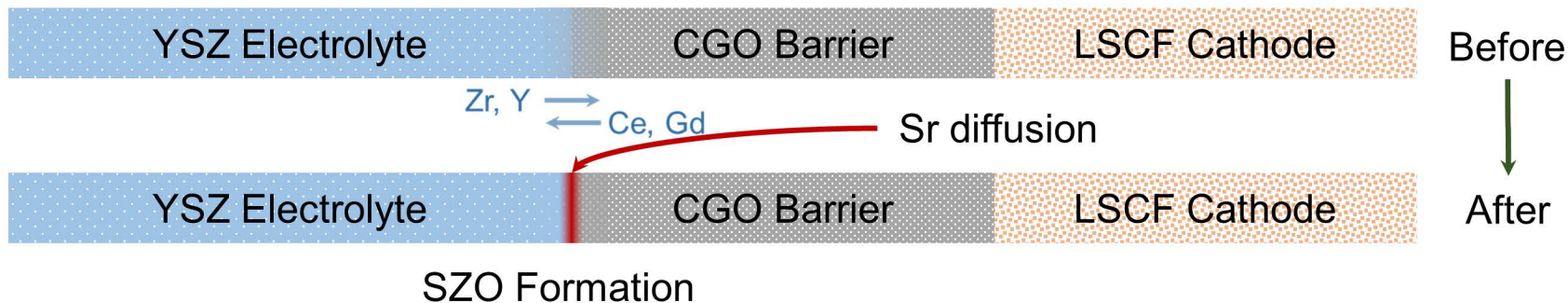
model for the simulation of the $\text{ZrO}_2\text{-CeO}_2\text{-SrO}$ system in the case of screen-printed CGO barrier layer; (c) 1D numerical model for the simulation of the $\text{ZrO}_2\text{-CeO}_2\text{-SrO}$ system in the case of PLD CGO barrier layer; (d) Numerical model for 3D phase field simulation of the SZO formation in the case of PLD CGO barrier layer. For (b) and (c), the SrO layer is introduced as a virtual layer without thickness.

1

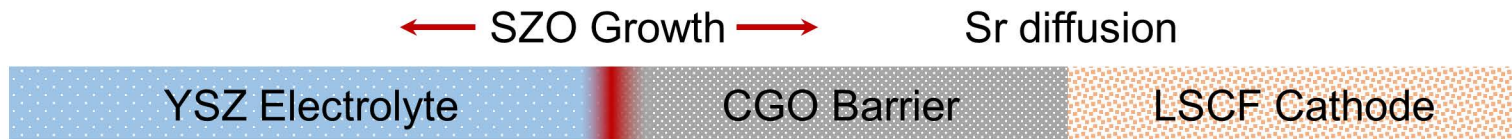
Step 1. Half-cell/Barrier Layer Sintering (1200 ~ 1350 °C)

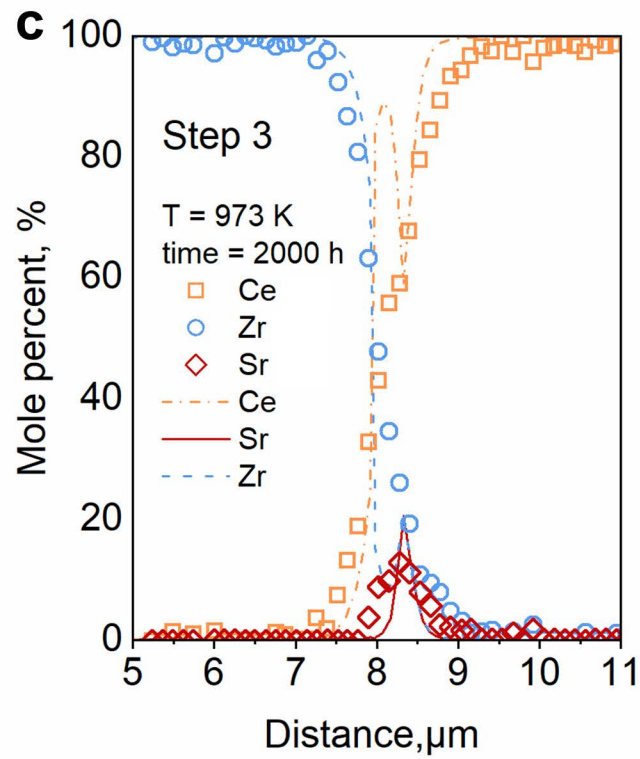
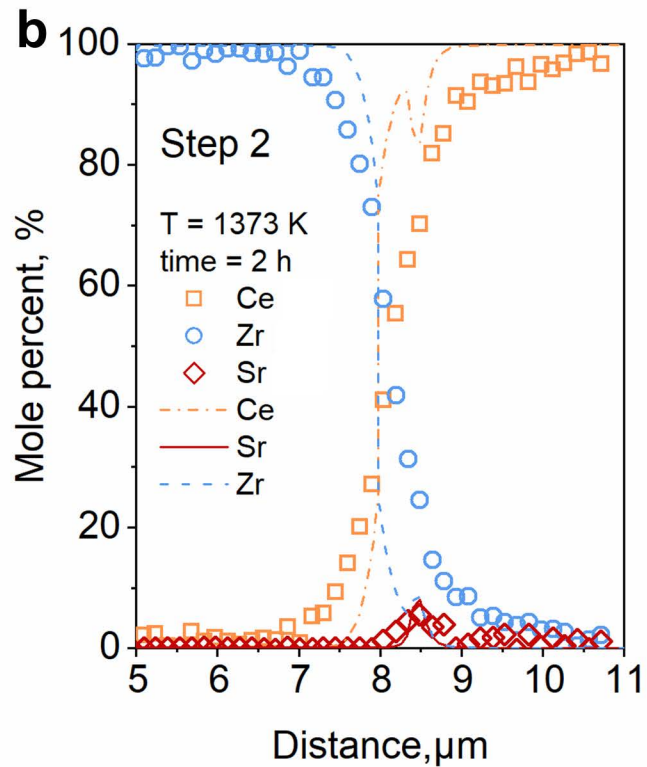
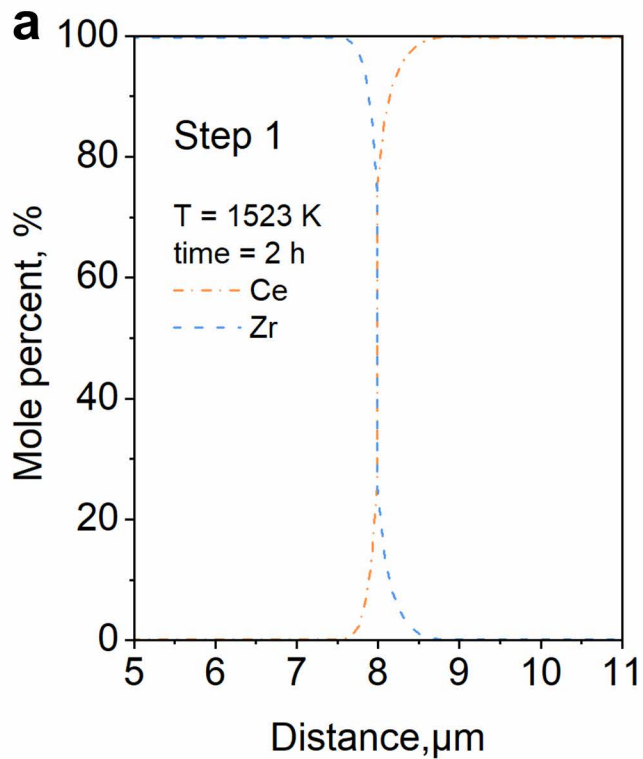


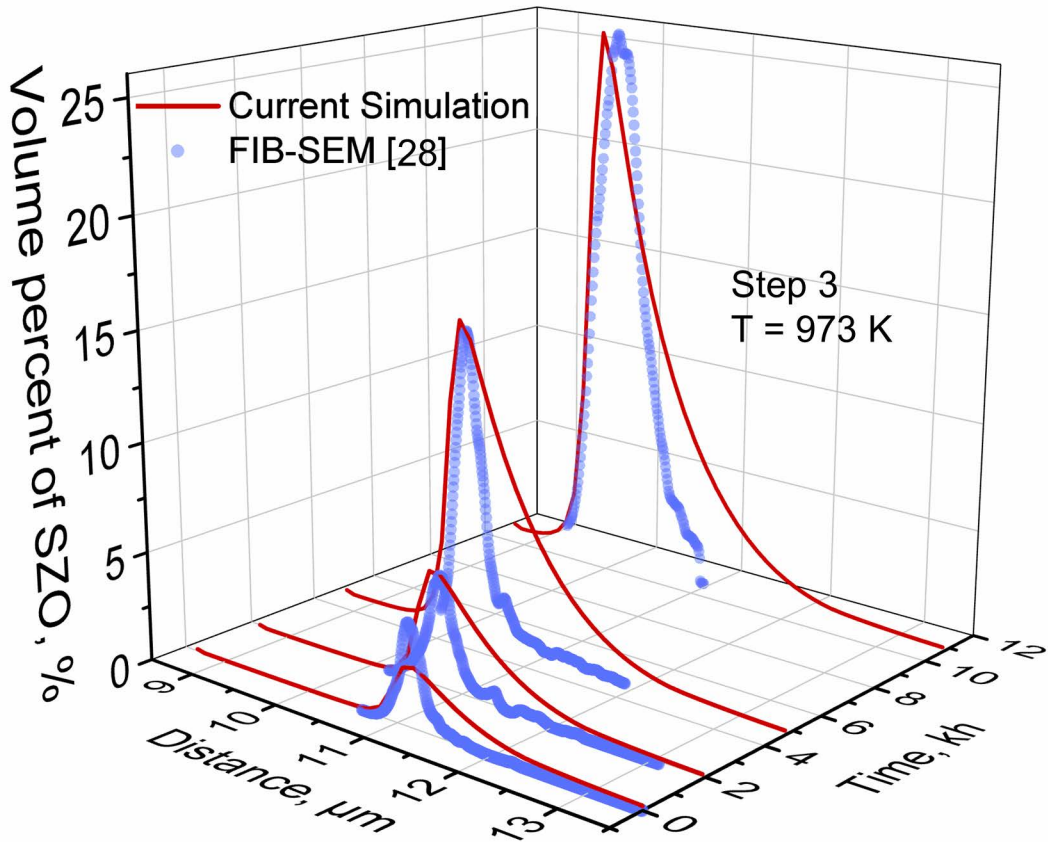
Step 2. Cathode Sintering (950 ~ 1150 °C)

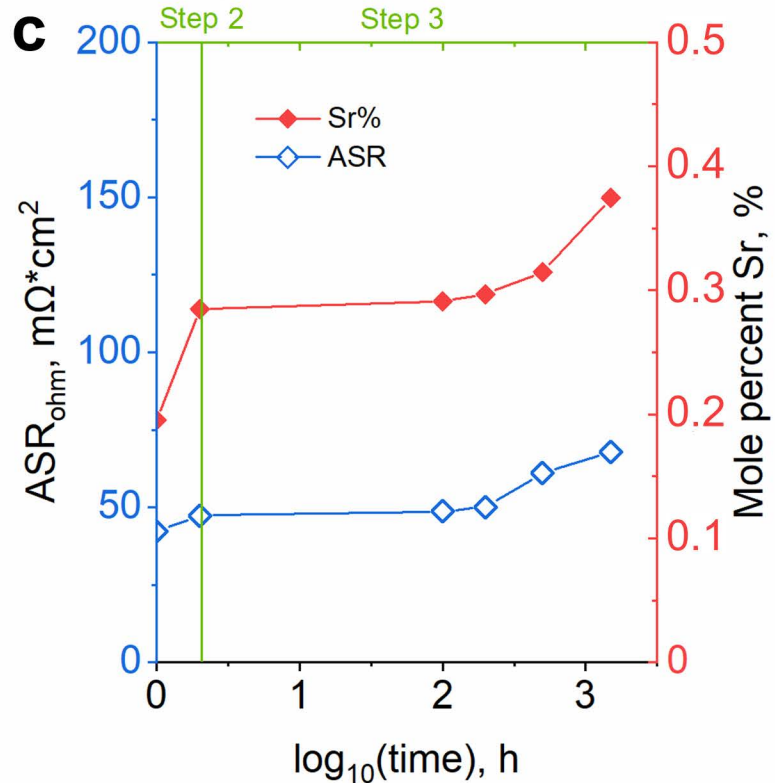
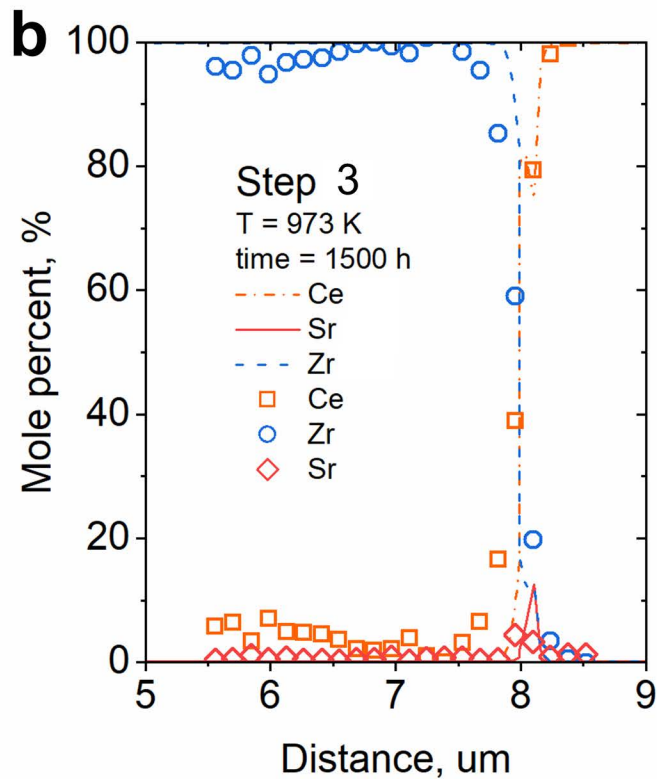
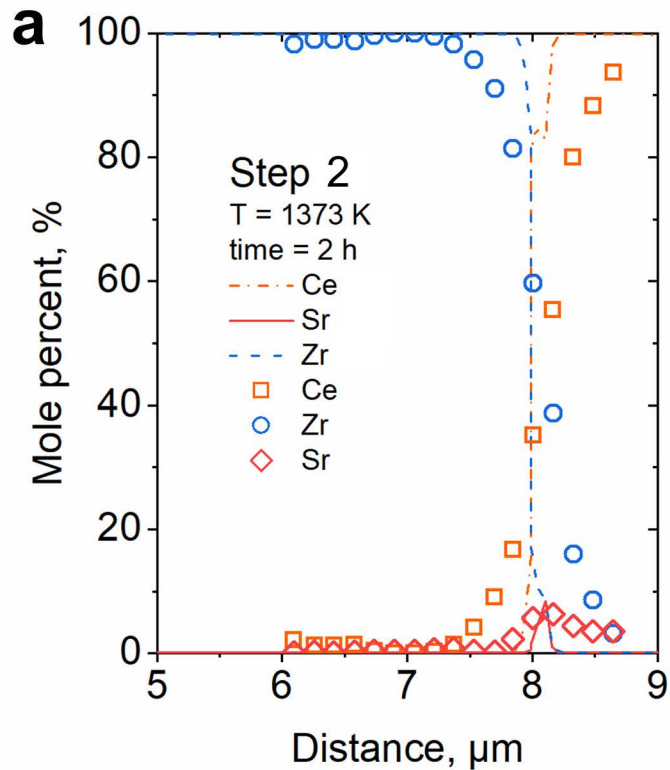


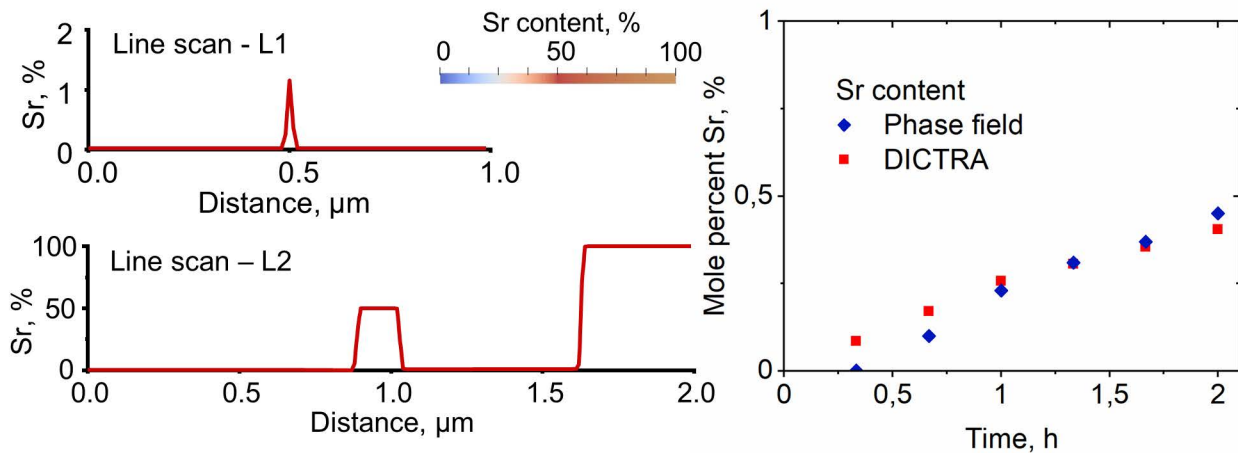
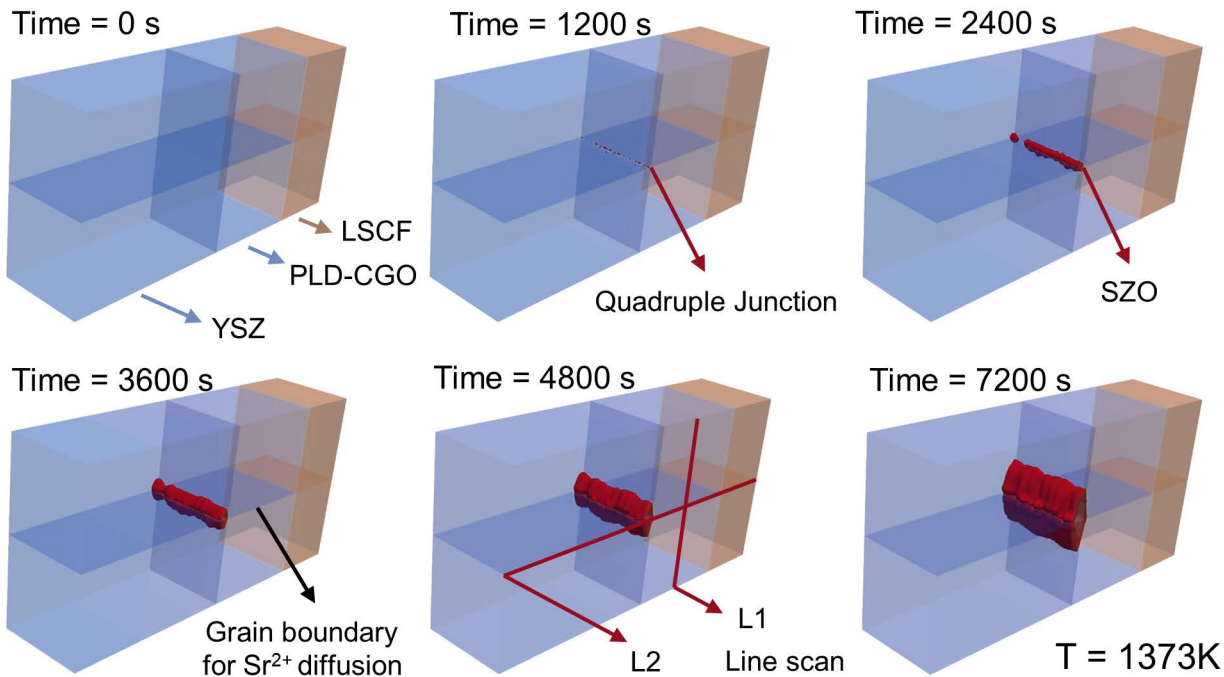
Step 3. Long-term Operation (650 ~ 750 °C)

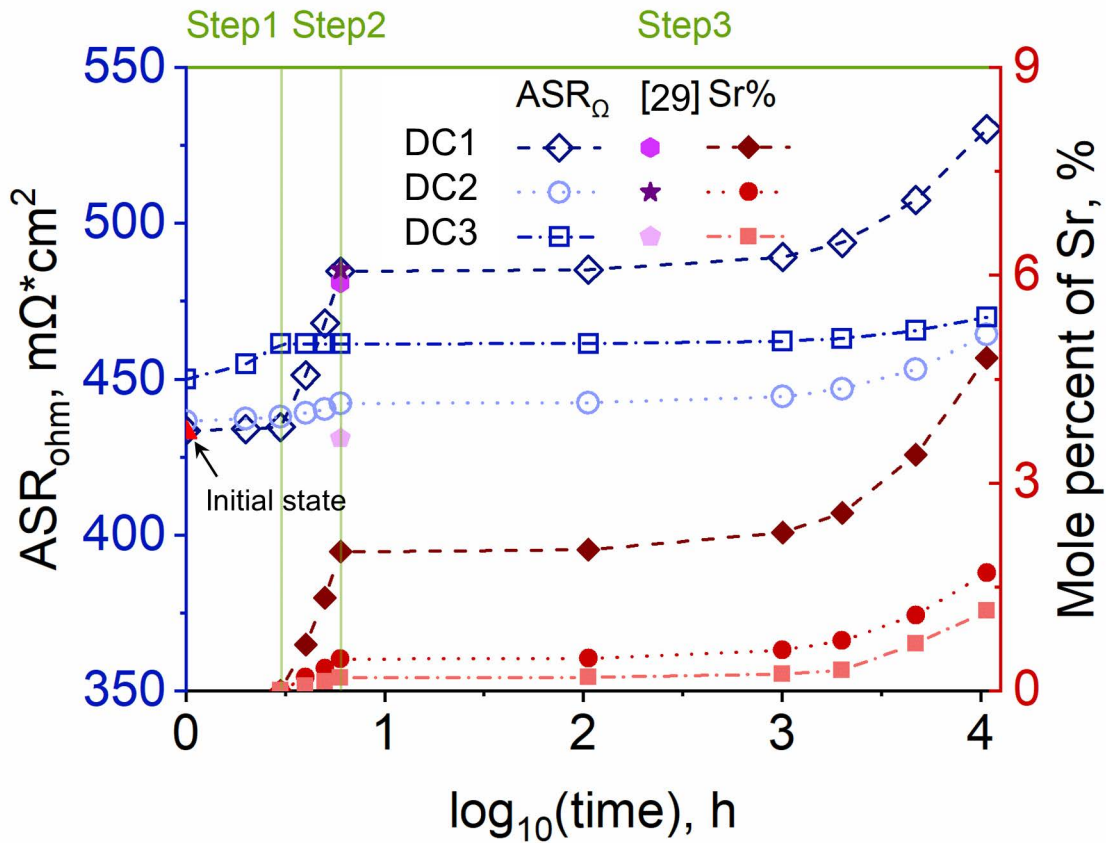


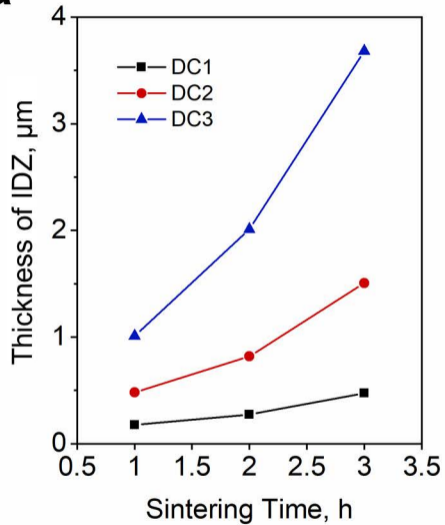
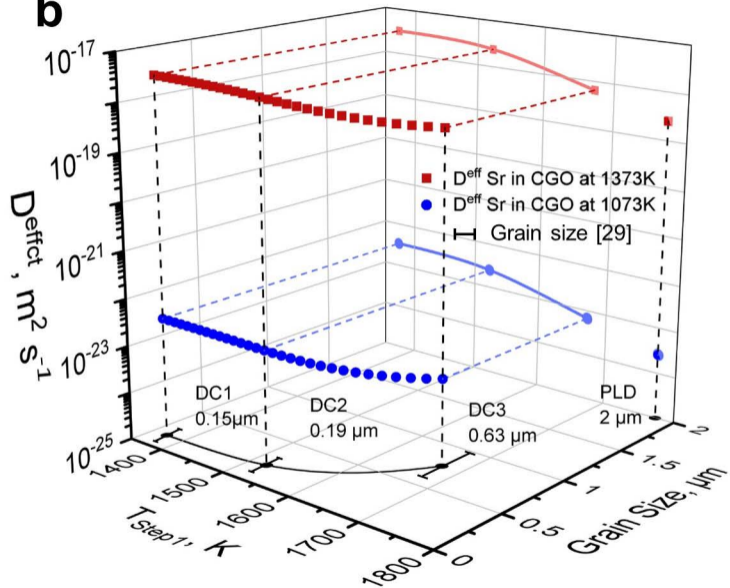


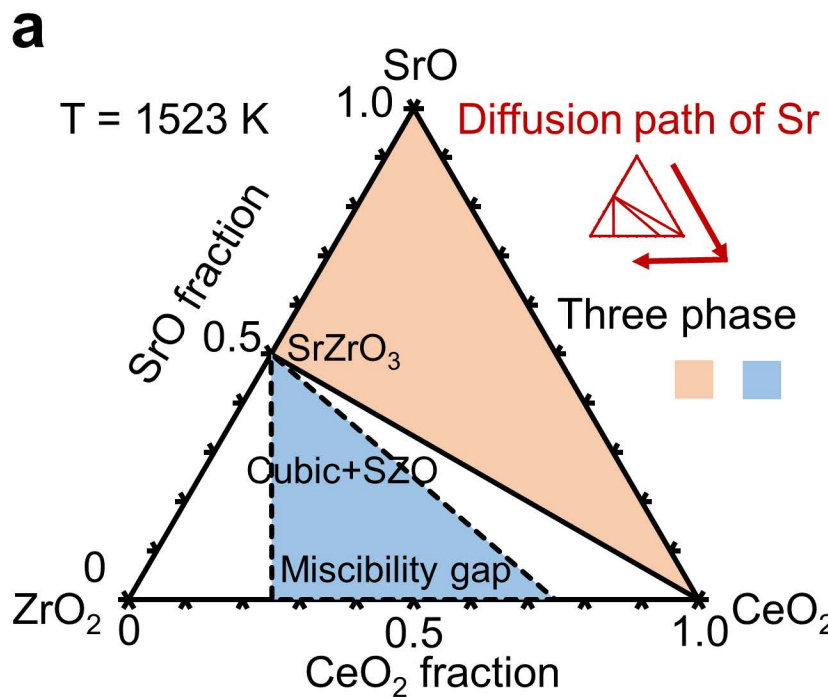




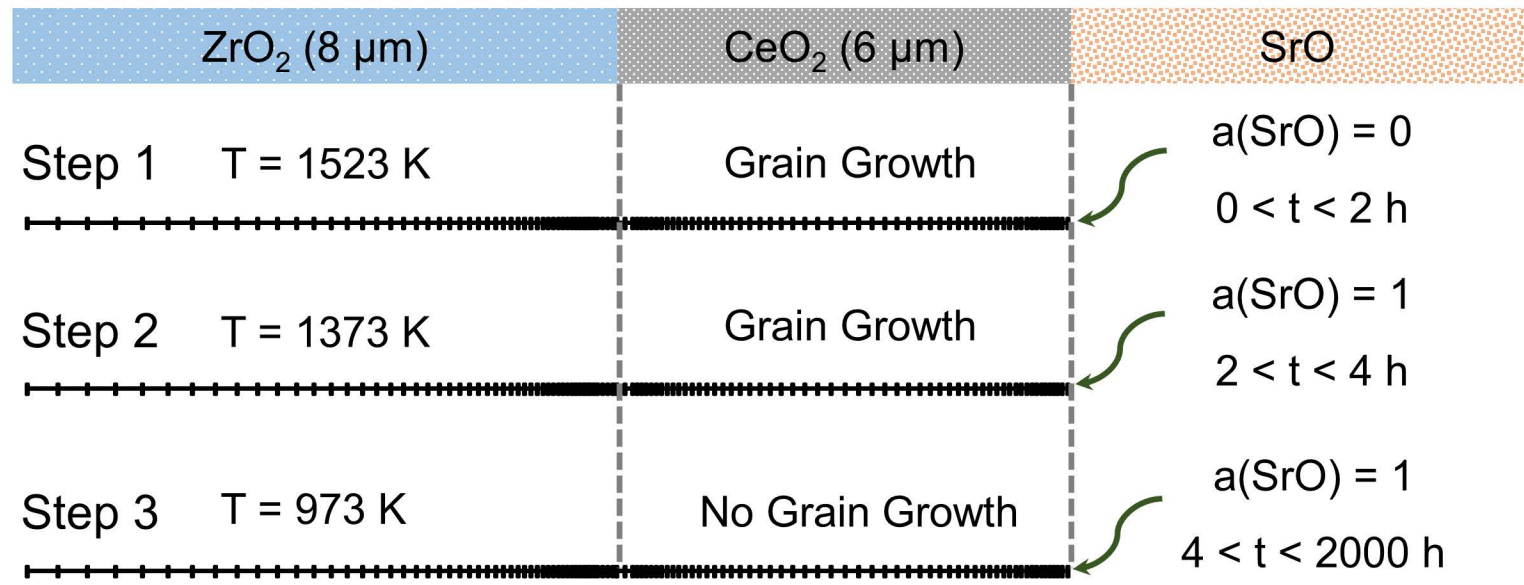




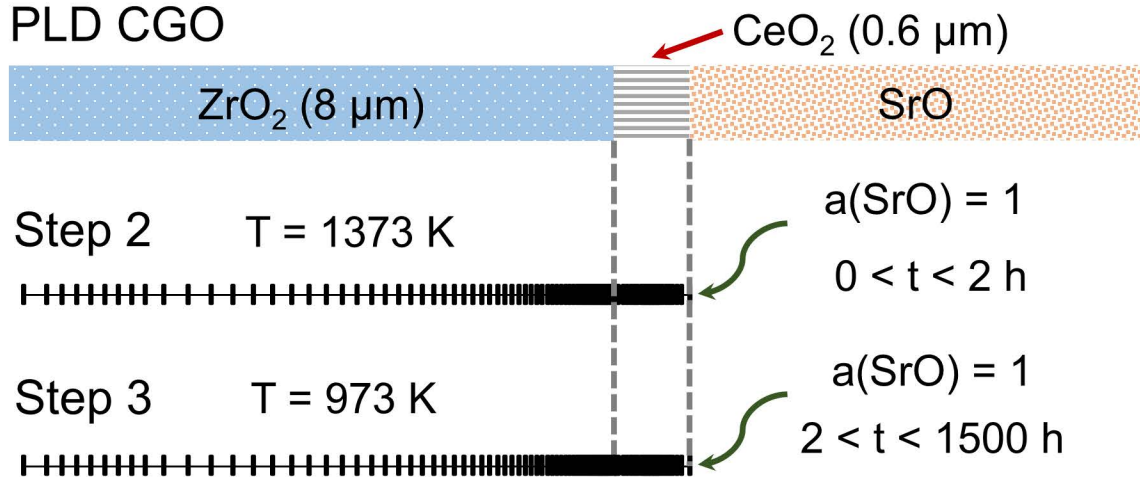
a**b**



b Screen Printed CGO



c PLD CGO



d PLD CGO (Step 2)

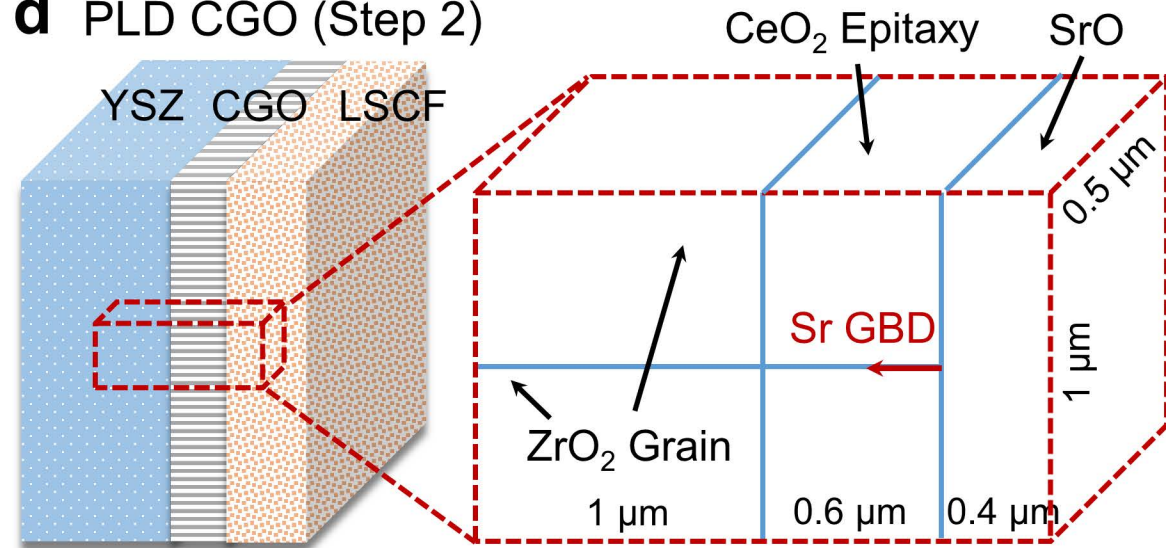


Table 1. Thermodynamic description of the ZrO₂-CeO₂-SrO system adopted in this work.

Phase	Description	Reference
Cubic	${}^0G_{(\text{Zr}^{4+})_1(\text{O}^{2-})_2}^{\text{Cubic}} = -1125234.1 + 496.72262T - 80T \ln T$	³⁷
(Ce ⁴⁺ ,Zr ⁴⁺) ₁ (O ²⁻) ₂	${}^0G_{(\text{Ce}^{4+})_1(\text{O}^{2-})_2}^{\text{Cubic}} = -1116114 + 429.345T - 72.0653T \ln T$ $- 0.0040536T^2 + 0.0040536T^{-1}$ ${}^0L^{\text{Cubic}} = 27797.69$	
SrO	${}^0G^{\text{SrO}} = -607870 + 268.9T - 47.36T \ln T - 0.00307T^2$	³⁸
(Sr ²⁺) ₁ (O ²⁻) ₁	$+ 190000T^{-1}$	
SZO	${}^0G^{\text{SZO}} = -1809275.23 + 733.05819T - 124.65927T \ln T$	³⁹
(Sr ²⁺) ₁ (Zr ⁴⁺) ₁ (O ²⁻) ₃	$- 0.0029230815T^2 + 1026060.9T^{-1}$	

Table 2. The elemental diffusivity data of the current ZrO₂-CeO₂-SrO system evaluated based on previous experimental data ⁴²⁻⁴⁵.

Diffusion component	D_0^{bulk} (m ² s ⁻¹)	Q^{bulk} (kJ mol ⁻¹)	D_0^{GB} (m ² s ⁻¹)	Q^{GB} (kJ mol ⁻¹)
Zr ⁴⁺ in YSZ ¹	4.1×10^{-6}	-434.2	4.1×10^{-6}	-286.9
Ce ⁴⁺ in YSZ	4.0×10^{-4}	-516.0	4.0×10^{-4}	-403.4
Sr ²⁺ in YSZ ²	8.9×10^{-4}	-601.5	8.9×10^{-4}	-466.1
Zr ⁴⁺ in CGO ¹	9.8×10^{-4}	-518.4	9.8×10^{-4}	-375.1
Ce ⁴⁺ in CGO ³	4.0×10^{-4}	-516.0	4.0×10^{-4}	-403.4
Sr ²⁺ in CGO	8.9×10^{-4}	-601.5	8.9×10^{-4}	-466.1

¹ Due to lack of experimental data, the grain boundary diffusivity is assumed to be 10⁵ times higher than the bulk diffusivity.

² Diffusivity of Sr²⁺ in YSZ is assumed to be the same as in CGO due to lack of experimental data.

³ Diffusivity of Ce⁴⁺ in CGO is assumed to be the same as in YSZ due to lack of experimental data.